Published online 26 September 2018 *Nucleic Acids Research, 2018, Vol. 46, No. 21* ***11287–11302***
doi: 10.1093/nar/gky875

Single-molecule DREEM imaging reveals DNA wrapping around human mitochondrial single-stranded DNA binding protein

Parminder Kaur[1,2,*], Matthew J. Longley[3], Hai Pan[1], Hong Wang[1,2] and William C. Copeland[3,*]

[1]Physics Department, North Carolina State University, Raleigh, North Carolina, NC 27695, USA, [2]Center for Human Health and the Environment, North Carolina State University, Raleigh, North Carolina, NC 27695, USA and [3]Genome Integrity and Structural Biology Laboratory, NIEHS, NIH, Research Triangle Park, NC 27709, USA

Received August 08, 2018; Revised September 13, 2018; Editorial Decision September 14, 2018; Accepted September 18, 2018

ABSTRACT

Improper maintenance of the mitochondrial genome progressively disrupts cellular respiration and causes severe metabolic disorders commonly termed mitochondrial diseases. Mitochondrial single-stranded DNA binding protein (mtSSB) is an essential component of the mtDNA replication machinery. We utilized single-molecule methods to examine the modes by which human mtSSB binds DNA to help define protein interactions at the mtDNA replication fork. Direct visualization of individual mtSSB molecules by atomic force microscopy (AFM) revealed a random distribution of mtSSB tetramers bound to extended regions of single-stranded DNA (ssDNA), strongly suggesting non-cooperative binding by mtSSB. Selective binding to ssDNA was confirmed by AFM imaging of individual mtSSB tetramers bound to gapped plasmid DNA substrates bearing defined single-stranded regions. Shortening of the contour length of gapped DNA upon binding mtSSB was attributed to DNA wrapping around mtSSB. Tracing the DNA path in mtSSB–ssDNA complexes with Dual-Resonance-frequency-Enhanced Electrostatic force Microscopy established a predominant binding mode with one DNA strand winding once around each mtSSB tetramer at physiological salt conditions. Single-molecule imaging suggests mtSSB may not saturate or fully protect single-stranded replication intermediates during mtDNA synthesis, leaving the mitochondrial genome vulnerable to chemical mutagenesis, deletions driven by primer relocation or other actions consistent with clinically observed deletion biases.

INTRODUCTION

Common enzymatic manipulation of DNA such as transcription, replication, repair and recombination requires the transient separation of DNA strands. Single-stranded DNA (ssDNA) generated during these transactions is vulnerable to attack by nucleases, chemical modification and the binding of inappropriate proteins. Single-stranded DNA binding proteins (SSBs) bind ssDNA with high selectivity and high affinity (1). Cells utilize SSBs to prevent the formation of secondary structures that interfere with normal maintenance processes and to protect against chemical and enzymatic degradation (2,3). SSBs serve critical roles in DNA metabolism by actively recruiting specific protein factors and participating in the coordinated assembly of protein–DNA complexes (4,5). They also stimulate DNA polymerase, helicase and strand exchange activities by facilitating ready access of enzymes to DNA substrates (6,7).

Mitochondrial DNA (mtDNA) is indispensable for cellular respiration and adenosine triphosphate production because it encodes several protein components that are required for electron transport and oxidative phosphorylation (8). Consequently, defects in mtDNA replication are a principle cause of severe and heritable metabolic disorders classified as mitochondrial diseases (9,10). Principle elements of the mtDNA replisome are DNA polymerase γ, the Twinkle mtDNA helicase and mitochondrial SSB (mtSSB) (11). mtSSB was first discovered in *Xenopus laevis* oocytes (12), and early work identified mtSSB as a major component of nucleoprotein fibers at displaced single-stranded loops of rat liver mtDNA (13). Cloning efforts permitted the isolation of *Xenopus*, rat, and human cDNAs en-

*To whom correspondence should be addressed. Tel: +1 984 287 4269; Fax: +1 919 541 4704; Email: copelan1@niehs.nih.gov
Correspondence may also be addressed to Parminder Kaur. Tel: +1 919 513 7203; Fax: +1 919 515 6538; Email: pkaur3@ncsu.edu

coding mtSSB. Predicted amino acid sequences show significant homology to *Escherichia coli* SSB and *E. coli* F conjugative plasmid SSB (14,15). The yeast *RIM1* gene encodes mtSSB and is essential for maintenance of mtDNA, as *rim1* null strains cannot grow on non-fermentable carbon sources and quickly become devoid of mtDNA (16). mtSSB is required for mtDNA replication and development in *Drosophila melanogaster* embryos (17) and cultured cells (18). Knockdown of mtSSB expression in cultured human cells reduces mtDNA synthesis and leads to a gradual decrease in mtDNA copy number with a more severe reduction in synthesis of 7S DNA (19).

The mtSSB is an essential component of the mtDNA replication machinery, and biochemical studies have demonstrated that cognate mtSSB proteins stimulate the activity of human pol γ (20,21) and *Drosophila* Pol γ (22,23) *in vitro*. Combining biochemical assays and electron microscopy (EM), a recent study demonstrated more directly that stimulation by mtSSB occurs by organizing the template DNA and eliminating secondary structure to favor ssDNA conformations that facilitate action by Pol γ (24). Human mtSSB has also been shown to stimulate the 5′-3′ unwinding activity of the Twinkle mtDNA helicase (21,25). In combination, Pol γ and Twinkle helicase function together on double-stranded DNA substrates to synthesize multi-kilobase DNA products, and addition of mtSSB significantly stimulates this minimal replisome *in vitro* (26). Also, Mikhailov and Bogenhagen demonstrated that mtSSB stimulates *X. laevis* Pol γ by enhancing processivity of DNA synthesis (27), similar to stimulation seen by direct interaction of T7 gp2.5 SSB with the T7 gp5 DNA polymerase–thioredoxin–gp4 helicase complex in the highly homologous bacteriophage T7 system (28). More recently, we demonstrated physical interaction between the C-terminal tail of the human NEIL1 DNA glycosylase and mtSSB *in vitro* in the presence or absence of DNA, which suggests coordinated action of the proteins during base excision repair of mtDNA (29).

Knowledge of the structure of mtSSB–DNA complexes is crucial to advance our understanding of the role of mtSSB in replication and repair of mtDNA, yet the crystal structure of mtSSB–ssDNA complexes has so far proven elusive. Based on fluorescence quenching data, tetrameric symmetry and the orientation of a positively charged channel on the crystal structure of unbound mtSSB, Kang and coworkers proposed a dynamic equilibrium between five distinct binding modes for ssDNA wrapping around the surface of mtSSB (30). Oliveira and Kaguni aligned the crystal structures of *E. coli* SSB bound to ssDNA and unbound human mtSSB to create a model of ssDNA bound to the presumptive DNA-binding groove of mtSSB (21). Both models are highly influenced by the structure of *E. coli* SSB. Recently, Qian and Johnson utilized FRET to assess bending of oligo$(dT)_{60}$ around mtSSB tetramers (31). We utilized atomic force microscopy (AFM) and the recently developed Dual-Resonance-frequency-Enhanced Electrostatic Force Microscopy (DREEM) technique (32) to investigate DNA binding by human mtSSB. We chose direct imaging by single-molecule techniques to eliminate the effects of ensemble averaging possible with bulk biochemical methods and to enable quantification of any structural heterogeneity in mtSSB–ssDNA samples. Uniquely, the DREEM technique simultaneously collects topographic and electrostatic force microscopy images and is capable of revealing distinct conformations in protein–DNA complexes, such as DNA wrapping around histones or the TRFH domain of the telomere binding protein TRF2, DNA passing through the DNA mismatch repair protein hMutSα, and higher order DNA looping at the edge of multi-protein TRF2–DNA complexes (32–34). Here, using AFM imaging in air, we observe that mtSSB predominantly exists in tetrameric complexes whether free or bound to DNA. We also find that mtSSB binds ssDNA substrates with limited cooperativity, although very low salt concentrations can infrequently induce the formation of short nucleoprotein filaments. DREEM imaging of mtSSB with various DNA substrates reveals a principle binding mode in which ssDNA wraps once around mtSSB. These results provide new insight into how mtSSB might influence DNA unwinding by Twinkle helicase and mechanisms underlying formation of mtDNA deletions through defective mtDNA replication.

MATERIALS AND METHODS

Single-stranded DNA binding proteins

The human SSBP1 cDNA encoding the mtSSB was overexpressed in *E. coli*, and recombinant human mtSSB was purified to homogeneity as described previously (35). Recombinant human mtSSB (15.3 kDa monomer form) was dialyzed into a buffer containing 30 mM HEPES-KOH (pH 7.6), 1 mM dithiothreitol, 0.25 mM ethylenediaminetetraacetic acid (EDTA), 0.25% (w/v) myoinositol, 0.01% (v/v) NP-40, 0.1 mM PMSF, 0.25 M KCl and 25% glycerol. Protein was quantified by UV absorbance at 280 nm utilizing an extinction coefficient (19 060 $M^{-1}cm^{-1}$ for monomers) calculated from the primary amino acid sequence (36,37), and stored at −20°C. *Escherichia coli* ssDNA binding protein (SSB) was purchased from Affymetrix.

DNA substrates

Circular single-stranded M13mp18 DNA (7249 nt) was prepared by overnight infection of *E. coli* XL1 Blue with M13mp18 viral particles at high MOI, followed by purification of viral particles by PEG8000 precipitation and CsCl density gradient centrifugation (average density 1.29 g/ml). Single-stranded M13mp18 DNA was extracted from viral particles with buffered phenol, dialyzed exhaustively and quantified by absorbance at 260 nm (38). Linear double-stranded DNA containing a 37-nt ssDNA gap was prepared by treating pSCW01 plasmid DNA (duplication of 2030 bp) provided by Peggy Hsieh (NIDDK) (39) with Nt.BstNBI to introduce four closely spaced nicks in one strand, incubating with complementary oligonucleotides at 68°C for 30 min followed by slow cooling to room temperature, and removing excess unbound oligonucleotides and short duplex DNA using 100K MW Amicon Ultra filtration columns (39,40). Gapped circular DNA was linearized by restriction

with ScaI, which positioned the 37-nt ssDNA gap 470 nt (23%, ∼160 nm assuming 0.34 nm/bp) from one end of the blunt-ended linear DNA fragment. Diagnostic restriction digestion of the gapped region indicated typical DNA gapping efficiencies of 85 to 95% (41). Circular double-stranded plasmid DNA containing a strand-specific 407-nt single-stranded gap was generated as described previously (42). Briefly, replicative form M13mp2 DNA was digested with PvuII restriction endonuclease, and gapped molecules were prepared by mixing single-stranded M13mp2 viral DNA (+ strand, 7196 nt) with the large PvuII fragment (6789 nt), followed by hybridization at 70°C.

Oligonucleotide substrates

DNA substrates utilized to assess DNA binding affinity were constructed from synthetic oligonucleotides. Two 40-nt oligomers D1 (5′- ATGCTAGCTTGGCTGTGA CTTTAAACCTGTCGTGCCAGCT -3′) and D2 (5′- AGCTGGCACGACAGGTTTAAAGTCACAGCC AAGCTAGCAT -3′) were obtained from Oligos Etc. (Wilsonville, OR, USA) and were quantified by absorbance at 260 nm. An internally modified version of D1 with fluorescein covalently attached to the thymine at position 21 (D1-F) was purchased from Sigma-Aldrich. The concentration of D1-F was determined spectrophotometrically at 260 nm and adjusted slightly downward to compensate for intrinsic absorbance of fluorescein at 260 nm (43). D1-F was utilized directly as an ssDNA substrate, whereas D1-F hybridized to the fully complementary oligonucleotide D2 served as the double-stranded DNA substrate. A 90-nt oligomer (5′- TAA TGC TAT CAC TAT TCG TAG ACT TGA CCA CAC CTT GTC AGC TCA CGC TCC AAA TGA AAG TAT AGC TAA ACA GGT TAT TGA CCA TAT GCA -3′) was obtained from Integrated DNA Technologies (IDT) and used as a ssDNA substrate for DREEM imaging. The same oligonucleotide bearing a 5-fluorescein adduct on the 5′-terminal thymine was utilized to assess DNA binding affinity by fluorescence anisotropy.

DNA binding assessed by fluorescence anisotropy

Fluorescent substrates were hybridized in a solution containing 10 mM Tris–HCl (pH 7.5), 50 mM NaCl, 0.1 mM EDTA and 10 μM each of the indicated oligonucleotides by heating to 85°C followed by slow cooling to room temperature. Immediately prior to use, the substrates were warmed to 42°C for 5 min and held at room temperature. Steady state fluorescence anisotropy was measured with an Olis RSM1000 spectrofluorometer (Bogart, GA) equipped with a 1.24 mm slit and a temperature-controlled cell set to 20°C. Incident light at the 480 nm excitation wavelength was horizontally plane polarized, and a photoelectric modulator was utilized to simultaneously measure horizontally and vertically plane-polarized fluorescence at 530 nm with a gated photon counting detector. Binding mixtures (0.2 ml) contained 30 mM HEPES-KOH (pH 7.5), 1 mM 2-mercaptoethanol, 5 mM $MgCl_2$, 0.01% NP-40, 50 mM NaCl and a 20 nM concentration of the specified fluorescein-conjugated oligonucleotide substrate. Intrinsic fluorescence of buffer components was undetectable at wavelengths relevant to fluorescein. Changes in fluorescence polarization were measured in response to the stepwise addition of purified mtSSB or *E. coli* SSB. Following a 1 min equilibration period after each addition, anisotropy data were collected in triplicate with a 10 s integration time. Changes in anisotropy were plotted against the total concentration of SSB, expressed as tetramers. To correct for the ligand depletion effect caused by non-trivial concentrations of protein–DNA complex relative to the total protein concentration, binding isotherms were fit to a quadratic equation by non-linear regression analysis to calculate apparent K_d(DNA) values (44). DNA binding cooperativity was estimated empirically from Hill plots (45).

Differential scanning fluorimetry

Protein stability was assessed by differential scanning fluorimetry with an Olis RSM1000 spectrofluorometer (Bogart, GA, USA) equipped with a gated photon counting detector and a temperature-controlled sample cuvette. Samples (0.2 ml) containing 30 mM HEPES-KOH (pH 7.5), 1 mM 2-mercaptoethanol, 50 mM NaCl, 4× SYPRO Orange (Molecular Probes) and 5.0 μM mtSSB (expressed as tetramers) were heated from 16°C to 92°C. SYPRO Orange fluorescence was measured with 470 nm excitation and 574 nm emission wavelengths, and fluorescence intensity was measured in quadruplicate with a 1 s integration time at 2°C increments. Progressive exposure of hydrophobic protein surfaces during thermal denaturation increases binding and fluorescence of the dye (46,47), and the thermal unfolding transition midpoint (T_m) was identified from the first derivative of the fluorescence signal as a function of temperature. Protein stability was also assessed by capillary-based differential scanning fluorimetry (Prometheus NT.48 instrument, NanoTemper Technologies). Changes in tryptophan fluorescence upon heating were monitored at 3 s intervals at 330 nm, and the thermal unfolding T_m was determined as before.

AFM sample preparation

To image free mtSSB (8.4 nM tetramers, 61.3 kDa), protein samples were diluted in Incubation Buffer containing 20 mM HEPES (pH 7.5) and 100 mM NaCl and were deposited onto a freshly cleaved mica surface. To assess DNA binding by mtSSB, the protein was first incubated with 3.6 nM M13mp18 ssDNA at various protein/DNA ratios (R = 2, 5, 10 and 20 mtSSB tetramer/DNA) at 37°C for 10 min in Incubation Buffer. Linear double-stranded DNA containing a 37-nt ssDNA gap (3.6 nM) or circular double-stranded DNA containing a 407-nt ssDNA gap (0.12 nM) was incubated with mtSSB (14.3 or 8.4 nM tetramers, respectively) under the same conditions. Single-stranded 90-nt oligonucleotides (159 nM) were incubated with mtSSB (80 nM) or *E. coli* SSB (80 nM) under the same conditions. All protein–DNA samples were diluted in AFM Imaging Buffer containing 20 mM HEPES (pH 7.5), 100 mM NaCl, 10 mM $Mg(OAc)_2$ and deposited onto a freshly cleaved mica surface. The mica surface was washed with deionized water followed by further drying with streams of nitrogen gas prior to imaging.

AFM and DREEM imaging and image analysis

AFM imaging in air was done using the AC mode on a MFP-3D-Bio AFM (Asylum Research) and Pointprobe® PPP-FMR cantilevers (Nanosensors, spring constants at ~2.8 N/m). All images were captured at a scan rate of 1–2 Hz and a resolution of 512 × 512 pixels. DREEM images were collected as described previously (32–34,48). Briefly, the AFM cantilever and the bottom of the mica substrate were coated with a thin layer of colloidal liquid silver (Ted Pella Inc.). A function generator (Sanford Research System, model DS335) was used to generate the AC bias at the first overtone and DC bias that were applied between the AFM cantilever and mica substrate. A lock-in-amplifier (Sanford Research System, model SR844 RF) was used to monitor the changes in vibration amplitude and phase at the first overtone as a function of sample positions. To optimize DREEM signals, AC and DC bias were adjusted from 0 to 20 V and −1.5 to 1.5 V, respectively. AFM volumes (mean ± standard deviation) of mtSSB alone and mtSSB–DNA complexes were measured using Gwyddion software. The types of AFM cantilevers and imaging conditions in this study matched our previous experiments relating molecular weight and AFM volume of proteins (34).

RESULTS

Conformation and stability of human mtSSB

The purification, purity and native conformation of recombinant human mtSSB was determined previously (35). Equilibrium sedimentation analysis in an Optima XL-A analytical ultracentrifuge yielded radial absorbance profiles at 280 nm that fit very well to a model of a single species with a molecular weight of 62 600 ± 1760 Da. Monomer and dimer forms were undetectable at protein concentrations from 11 to 32 μM mtSSB (monomer), permitting estimation of a subunit dissociation constant $<10^{-8}$ M. As the predicted molecular weight of recombinant mtSSB is 15 316 Da, the measured value indicates that recombinant human mtSSB is a tetramer in solution (35), as observed previously for native and recombinant forms of mtSSB from *X. laevis* (27,49), *D. melanogaster* (50) and humans (37).

The stability of mtSSB was assessed by differential scanning fluorimetry ('Materials and Methods' section). Samples of mtSSB were mixed with the hydrophobic fluorescent probe SYPRO Orange, and thermal denaturation of the protein was gauged by monitoring fluorescence intensity as the mixture was heated from 16°C to 92°C (Supplementary Figure S1). The thermal unfolding profiles exhibited single, distinct transitions with an average T_m of 72.5 ± 1.1°C. Protein stability in the absence of dye was judged by changes in tryptophan fluorescence upon heating from 20°C to 95°C ('Materials and Methods' section), and mtSSB again exhibited a single, narrow transition with a T_m of 74.1°C. The abrupt denaturation of mtSSB indicates a uniform population of molecules, and a moderately high T_m suggests human mtSSB occupies a thermally stable conformation in solution. Murine mtSSB has also been shown to exhibit remarkable thermal stability, and previous experiments demonstrated that temperatures >60°C were needed to disrupt the non-covalent association of wild-type mtSSB monomers and that tetramer disassociation likely preceded denaturation of individual mtSSB monomers (51).

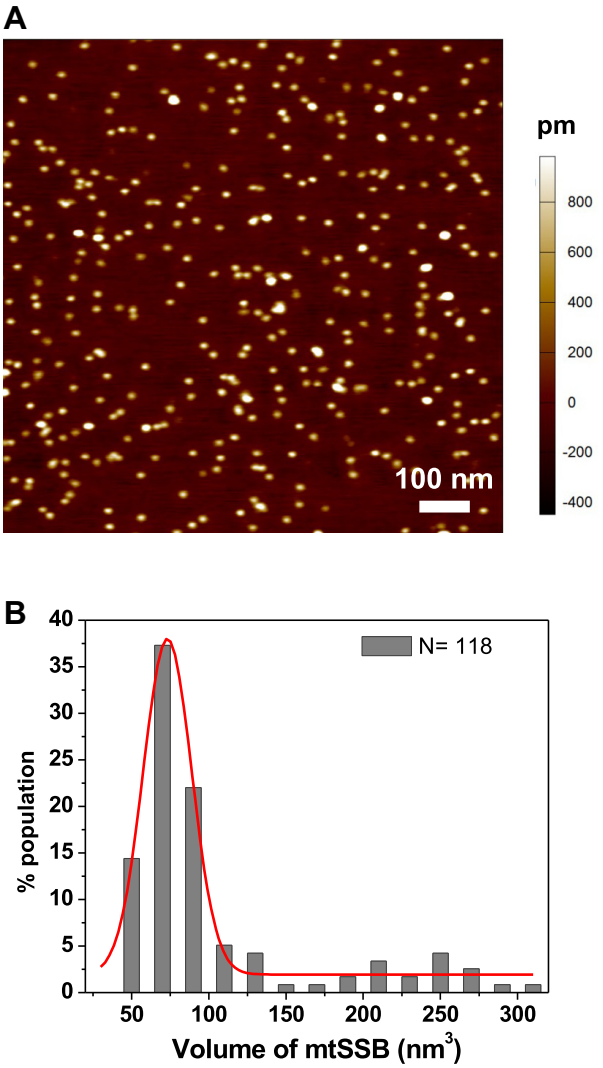

Figure 1. AFM volume measurement shows the formation of mtSSB tetramers. (**A**) A representative AFM topography image of mtSSB (8.4 nM) on a mica surface obtained using the AC imaging mode, as described in 'Materials and Methods' section. (**B**) AFM volume distribution (N = 118) of the human mtSSB protein fit with a Gaussian function (red line, $R^2 = 0.95$) with a peak centered at 73.2 (±31.4) nm^3.

Human mtSSB was also assessed by direct imaging using AFM imaging in air. Samples of mtSSB protein (8.4 nM tetramer) were applied to freshly cleaved mica surfaces ('Materials and Methods' section). A nearly uniform field of particles is readily apparent (Figure 1A), and estimating the AFM volume of individual mtSSB complexes reveals a Gaussian distribution centered at 73.2 (±31.4) nm^3 (Figure 1B). Based on the standard calibration curve ($V = 1.45$ MW – 21.59) that linearly correlates AFM volumes (V) of globular proteins with their molecular weights (MW) (34), the AFM volume of mtSSB corresponds to a protein complex with a molecular weight of ~65 kDa. Consistent with previous studies employing ultracentrifugation, EM and X-ray crystallography (30), our AFM measurements directly

demonstrate that free human mtSSB exists as tetramers in solution.

DNA binding affinity of recombinant human mtSSB

Electrophoretic Mobility Shift Assay (EMSA)analysis demonstrated that *X. laevis* mtSSB (*Xl*-SSB) could efficiently bind DNA oligonucleotides as short as dT_{32} and that dT_{68} could accommodate binding of two *Xl*-SSB tetramers (27). Accordingly, we utilized fluorescence polarization methods to quantify the binding affinity of human mtSSB to various DNA substrates with free and bound species at equilibrium in solution ('Materials and Methods' section). Fluorescein-labeled single-stranded or double-stranded DNA substrates were mixed with increasing concentrations of mtSSB, and formation of protein–DNA complexes was monitored by the increase in fluorescence anisotropy (Supplementary Figure S2). Plotted isotherms were fit to the quadratic binding equation to estimate equilibrium binding constants. Human mtSSB tetramers exhibited a $K_{d(ssDNA)}$ of 1.8 ± 0.9 nM on the 40-nt ssDNA substrate, and binding to the double-stranded DNA substrate was undetectable. As expected, mtSSB tetramers displayed preferential, high-affinity binding to ssDNA, consistent with the binding specificity of the *D. melanogaster* mtSSB (50,52). Comparable binding affinities of *D. melanogaster* mtSSB (K_d = 1.7 ± 0.06 nM) and human mtSSB (K_d = 2.3 ± 0.07 nM) for a 40 base oligonucleotide were determined by EMSA in the presence of 30 mM KCl (24). Also, the binding affinity of human mtSSB (K_d = 3.8 nM) for a 48 base oligonucleotide was determined by EMSA in the presence of 4 mM $MgCl_2$ and 50 mM NaCl (21). The binding affinities of *E. coli* SSB for oligo$(dT)_{16}$ (K_d = 1.67 μM) and oligo$(dT)_{30–40}$ ($K_d \leq$ 2.0 nM) were determined by fluorescence methods (53).

To minimize the influences of different methods, solution conditions, DNA lengths and base compositions on binding affinity, we determined binding affinities of human mtSSB and *E. coli* SSB for a 90-nt ssDNA substrate under identical conditions. In the presence of 5 mM $MgCl_2$ and 50 mM NaCl, human mtSSB had a $K_{d(ssDNA)}$ of 14.7 ± 0.5 nM with this oligonucleotide (Figure 2A), whereas *E. coli* SSB also exhibited high-affinity binding with a $K_{d(ssDNA)}$ of 25.4 ± 1.3 nM (Figure 2B). The non-random distribution of residual values for both mtSSB and *E. coli* SSB showed deviation from a simple model for equilibrium binding. We replotted binding values in Hill plots (Figure 2C) to assess whether cooperative DNA binding was contributing to this apparent non-ideality. Linear curve fitting generated Hill coefficients of 2.00 for mtSSB and 1.84 for *E. coli* SSB, indicating that multiple SSB tetramers were binding to some of the 90-nt ssDNA molecules. Because our solution conditions favor an average occluded binding site size of ~60 nt (31,37), this mathematical analysis cannot distinguish limited cooperative binding from multiple independent binding events on a given oligonucleotide. Also, we note that equations used to estimate cooperativity in bulk mixtures assume that binding is both reversible and at equilibrium, which may not always be the case for SSBs. Accordingly, we turned to single-molecule imaging techniques to further examine the modes of mtSSB binding to various DNA substrates.

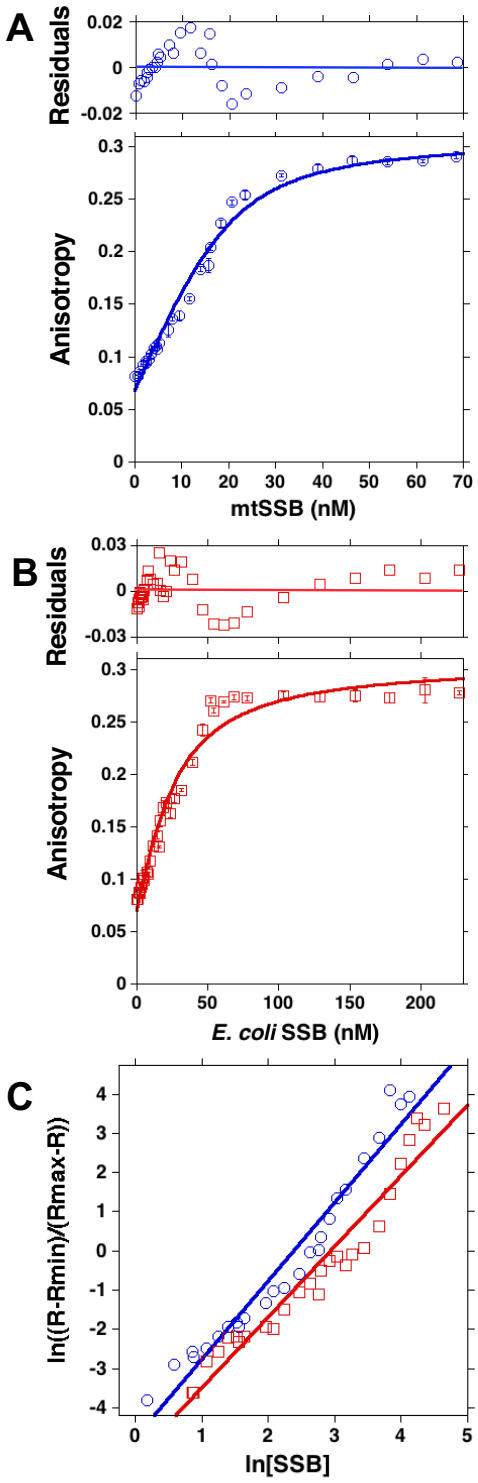

Figure 2. DNA binding affinity of mtSSB and *Escherichia coli* SSB. Changes in fluorescence anisotropy of a fluorescein-conjugated 90-nt oligonucleotide substrate were measured in response to the step-wise addition of (**A**) mtSSB or (**B**) *E. coli* SSB proteins, as described in 'Materials and Methods' section. Binding buffer contained 30 mM HEPES-KOH (pH 7.5), 1 mM 2-mercaptoethanol, 5 mM $MgCl_2$, 0.01% NP-40, 50 mM NaCl, 20 nM oligonucleotide and the indicated amounts of proteins. Protein concentrations are expressed as tetramers. Error bars are standard deviations of triplicate determinations. (**C**) DNA binding cooperativity was estimated by replotting binding data for mtSSB (blue circles) and *E. coli* SSB (red squares) as a Hill plot.

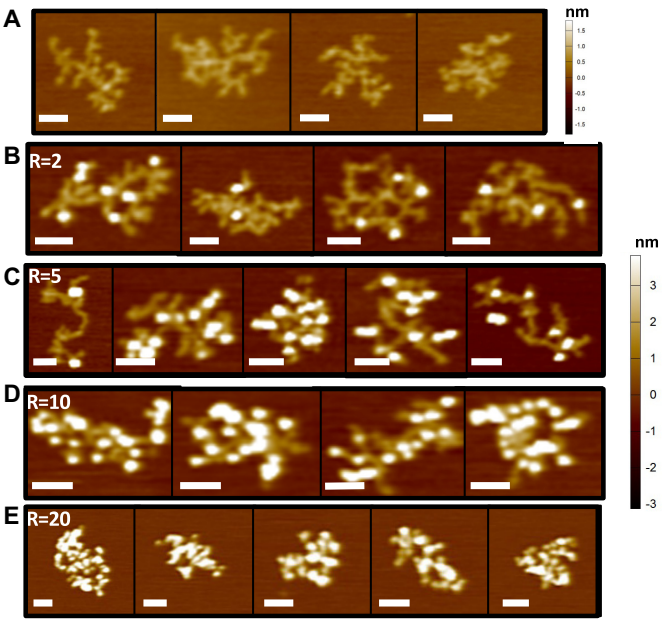

Figure 3. MtSSB binding to ssDNA is not cooperative. AFM topographic images were collected for (**A**) circular single-stranded M13mp18 DNA (7249 nt), and (**B**–**E**) mtSSB bound to single-stranded M13mp18 DNA at stoichiometric ratios (R = mtSSB tetramer/M13mp18 DNA) of (B) $R = 2$, (C) $R = 5$, (D) $R = 10$ or (E) $R = 20$. X-Y scale bar = 50 nm. Samples were incubated in Incubation Buffer containing 20 mM HEPES (pH 7.5) and 100 mM NaCl at 37°C for 10 min and imaged in AFM Imaging Buffer containing 20 mM HEPES (pH 7.5), 100 mM NaCl, 10 mM $Mg(OAc)_2$ as described in 'Materials and Methods' section.

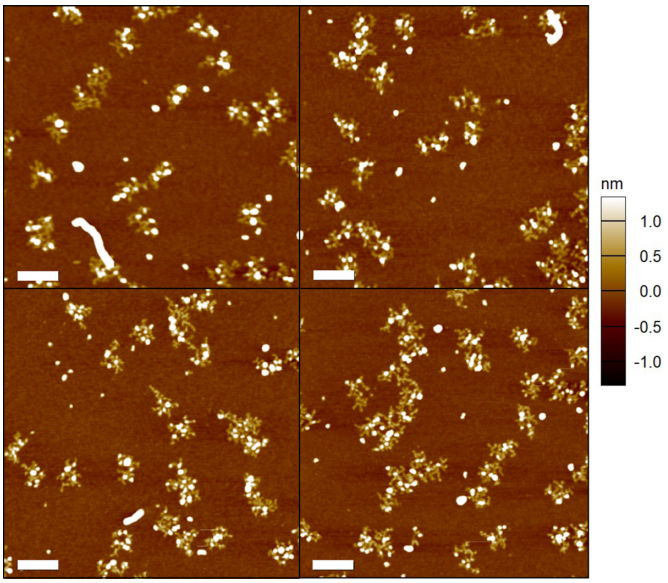

Figure 4. AFM images of *Escherichia coli* SSB bound to single-stranded M13mp18 DNA. AFM topographic images were collected for *E. coli* SSB (8.4 nM) interacting with circular single-stranded M13mp18 DNA (7249 nt) at a stoichiometric ratio of 10 *E. coli* SSB tetramers/M13mp18 DNA. Samples were incubated in Incubation Buffer containing 20 mM HEPES (pH 7.5) and 100 mM NaCl at 37°C for 10 min and imaged in AFM Imaging Buffer containing 20 mM HEPES (pH 7.5), 100 mM NaCl, 10 mM $Mg(OAc)_2$ as described in 'Materials and Methods' section. X-Y scale bar = 200 nm.

mtSSB binds ssDNA with limited cooperativity

Earliest observations of protein–mtDNA complexes isolated from rat liver mitochondria first identified mtSSB, and electron micrographs of glutaraldehyde crosslinked complexes revealed 'nucleoprotein fibers' within displacement loops of rat liver mtDNA (13). Restriction analysis localized 80% of nucleoprotein fibers to D-loops and expanded D-loops (13), consistent with early EM studies of mtDNA replication intermediates in mouse L cells (54). In contrast, electron micrographs from later experiments showed a near random distribution of purified recombinant mtSSB tetramers bound to individual poly(dT) strands, suggesting low cooperativity when binding multiple mtSSB tetramers at 300 mM NaCl (37). To understand the factors affecting these apparent differences in binding cooperativity, we bound human mtSSB to single-stranded circular M13mp18 DNA (7249 nt) without chemical crosslinking and directly visualized protein–DNA complexes using AFM (see 'Materials and Methods' section). Naked M13mp18 DNA in AFM Imaging Buffer containing 100 mM NaCl is sufficiently mobile to adopt dynamic conformations, and individual DNA molecules with regions containing secondary structures are clearly distinguishable on the mica surface (Figure 3A). Binding of mtSSB to M13mp18 DNA at low stoichiometric ratios resulted in a random distribution of mtSSB molecules along the DNA (Figure 3B and C). The AFM heights for single-stranded M13mp18 DNA alone (including regions with limited secondary structure) is 0.70 (±0.34) nm ($N = 100$), and mtSSB bound to M13mp18 DNA is unambiguously identified by a distinct AFM height of 2.41 (±0.56) nm ($N = 100$, Supplementary Figure S3a). The AFM volume distribution of mtSSB bound to ssDNA peaked at 137.5 (±42.6) nm^3 (Supplementary Figure S3b), which is greater than the volume of free mtSSB tetramers in solution ($73.2 \pm 31.4\ nm^3$, Figure 1B) due to inclusion of ssDNA. Higher mtSSB protein/DNA ratios proportionately increased the density of bound mtSSB molecules, yet complexes remained distinct and did not form the nucleoprotein tracts that are a hallmark of cooperative DNA binding (Figure 3D and E). Although regions of ssDNA between mtSSB–ssDNA complexes were not resolved in the electron micrographs of a previous study (37), AFM imaging clearly shows DNA between individually bound mtSSB complexes (Figure 3). In fact, correlating AFM topography, amplitude and phase data channels permitted us to quantify the volume and number of mtSSB complexes interacting with each single-stranded M13mp18 DNA molecule (Supplementary Figure S3c and d).

DNA binding by *E. coli* SSB has been extensively characterized. *Escherichia coli* SSB has been shown to bind ssDNA with unlimited cooperativity at low (<20 mM NaCl) salt concentrations and with limited cooperativity at higher (>100 mM NaCl) salt concentrations (55,56). When we assessed binding of *E. coli* SSB to M13mp18 DNA by AFM in imaging buffer containing 100 mM NaCl, *E. coli* SSB-M13 DNA complexes were divided into two populations. The majority of *E. coli* SSB tetramers were bound in a distributed fashion (Figure 4), as expected for this buffer and binding density (10 SSB tetramers/M13mp18 DNA). However, single-molecule imaging also allowed us to de-

tect nucleoprotein filaments in 3.3% ($N = 582$) of protein–DNA complexes. In some cases, *E. coli* SSB coated the entire length of M13mp18 DNA molecules when unbound DNA molecules were present in the same image (Figure 4), which was an indication of highly cooperative binding in a fraction of *E. coli* SSB–M13mp18 DNA complexes. Our results are comparable to previous experiments that utilized much higher ratios of *E. coli* SSB/DNA and documented highly cooperative DNA binding as assessed by EM (57) and by AFM (58,59). We also determined the binding mode of mtSSB and *E. coli* SSB to M13mp18 DNA under low salt conditions. In imaging buffer containing 20 mM NaCl, mtSSB continued to exhibit distributed binding to single-stranded M13mp18 DNA, although at this reduced salt concentration 3.0% ($N = 470$) of the mtSSB–DNA complexes appeared as nucleoprotein filaments (Supplementary Figure S4). In comparison, nucleoprotein filaments were present in 8.9% ($N = 751$) of *E. coli* SSB-M13mp18 DNA complexes formed under identical conditions (Supplementary Figure S5). Thus, reducing the salt concentration to 20 mM NaCl increased the incidence of nucleoprotein filaments for both proteins. Although the measured AFM heights of mtSSB-M13 DNA filaments and *E. coli* SSB-M13 DNA filaments are essentially the same, the lengths of *E. coli* SSB-M13 DNA filaments are more broadly distributed and have an average length (128.8 ± 52.5 nm, $N = 67$) notably greater than those formed by mtSSB (91.7 ± 36.3 nm, $N = 20$) at 20 mM NaCl (Supplementary Figure S6). The specific structural features of mtSSB that favor formation of short filaments only at low salt concentrations are unclear. However, the variable prevalence and length of nucleoprotein filaments for mtSSB and *E. coli* SSB implies the decrease in salt concentration needed to trigger cooperative DNA binding may differ for the two proteins. Taken together, our observations suggest that compared to *E. coli* SSB, mtSSB displays more limited cooperativity for binding ssDNA, especially at physiological salt concentrations.

mtSSB tetramer binding to ssDNA gaps induces DNA shortening

The apparent low cooperativity of DNA binding by mtSSB prompted us to suspect other fundamental differences in DNA binding between mtSSB and *E. coli* SSB. Binding to poly(dT) quenches the intrinsic tryptophan fluorescence of human mtSSB tetramers, and titration experiments indicated an average occluded binding site size of 50–70 nt at salt concentrations between 0.05–2.0 M NaCl. Modeling based on stopped-flow kinetics was consistent with an initial binding site length of ≤15 nt with rapid reshuffling to an equilibrium binding site size of 60 nt (37). Other studies employing fluorescence quenching suggested that *Drosophila* mtSSB binds ssDNA longer than 17 nt under low salt conditions, and EMSA competition analyses suggested a binding site of 25–32 nt in length (50). EMSA analysis demonstrated that *X. laevis* mtSSB could efficiently bind DNA homopolymers and oligomers as short as dT_{32} (27). Qian and Johnson extended these fluorescence titrations to reveal occluded site sizes on poly(dT) in the presence of 10 mM $MgCl_2$ of ∼28 nt at 20 mM NaCl and ∼60 nt at >200 mM NaCl. Binding kinetics at physiological salt concentrations identified a transient site size of 30 nt that rapidly transitions to a more fully wrapped mode with an equilibrium binding site size of 60 nt (31). These previous bulk biochemical assessments yielded a broad range for the size of the DNA binding site for mtSSB, possibly due to DNA sequence differences in the chosen substrates or the averaging of specific and non-specific DNA binding events (60). Accordingly, we employed AFM to visualize directly mtSSB bound to specific DNA substrates with defined regions of ssDNA. We generated a linear DNA substrate containing a site-specific 37-nt ssDNA gap flanked by double-stranded DNA arms (Figure 5A). AFM analysis shows that mtSSB predominantly binds at a position 22.6% (±4.6%) from one blunt end of the linear, gapped 2030 bp DNA substrate, which corresponds to the position of the ssDNA gap (∼23%, Figure 5B and C). Analysis of the fractional occupancies (60) of mtSSB on the DNA containing the 37-nt gap reveals that mtSSB displays a high binding specificity ($S = K_{SP}/K_{NSP} = 1.45 \times 10^4$) for the ssDNA gap. The calculated AFM volume of mtSSB particles bound to ssDNA in the gapped region was 113.8 (±86.9) nm^3 (Figure 5D), which is slightly smaller than what was observed on single-stranded M13mp18 DNA (137.5 ± 42.6 nm^3, Supplementary Figure S3b). The AFM volume of the ssDNA in the 37-nt gapped region was estimated to be ∼45 nm^3, assuming AFM height of 0.35 nm, width of 7 nm and length of 18.5 nm (0.5 nm/nt). Subtracting these values predicts the AFM volume of the protein component of mtSSB–ssDNA complexes is ∼68 nm^3, which correlates well with the AFM volume of individual mtSSB tetramers (73.2 ± 31.4 nm^3; Figure 1B). Strikingly, the binding of mtSSB tetramers to the ssDNA gap significantly shortens the contour length of linear gapped DNA (Figure 5E). Ungapped linear plasmid DNA (2030 bp) in our AFM images has a contour length of 671.0 (±26.4) nm. Gapped linear DNA has a slightly shorter contour length of 663.8 (±19.4) nm, suggesting limited folding or compaction of ssDNA within the gapped region. Upon binding mtSSB, the contour length of the linear gapped DNA was shortened further to 650.8 (±15.7) nm (Figure 5E). In a previous AFM study of UvrB, the shortening of DNA contour length upon binding to protein was attributed to DNA wrapping around the protein (61). Assuming that fully extended ssDNA has a step size of 0.5 nm per base (62), a similar analysis of ssDNA wrapping around mtSSB predicts that the observed ∼20 nm shortening of DNA contour length corresponds to ∼40 nt of ssDNA wrapping around one mtSSB tetramer. Taken together, direct AFM imaging of mtSSB–ssDNA complexes strongly supports the notion that DNA contour length shortens upon binding mtSSB due to ssDNA wrapping around mtSSB tetramers.

DREEM imaging directly reveals the DNA path wrapping around mtSSB

Based on the crystal structure of human mtSSB, Kang and co-workers noted four distinct positively charged patches forming a channel flanked by β-hairpin loops on the surface of the mtSSB tetramer, leading them to propose five distinct mtSSB DNA binding modes in a dynamic equilibrium (30). To determine the population distribution of different DNA

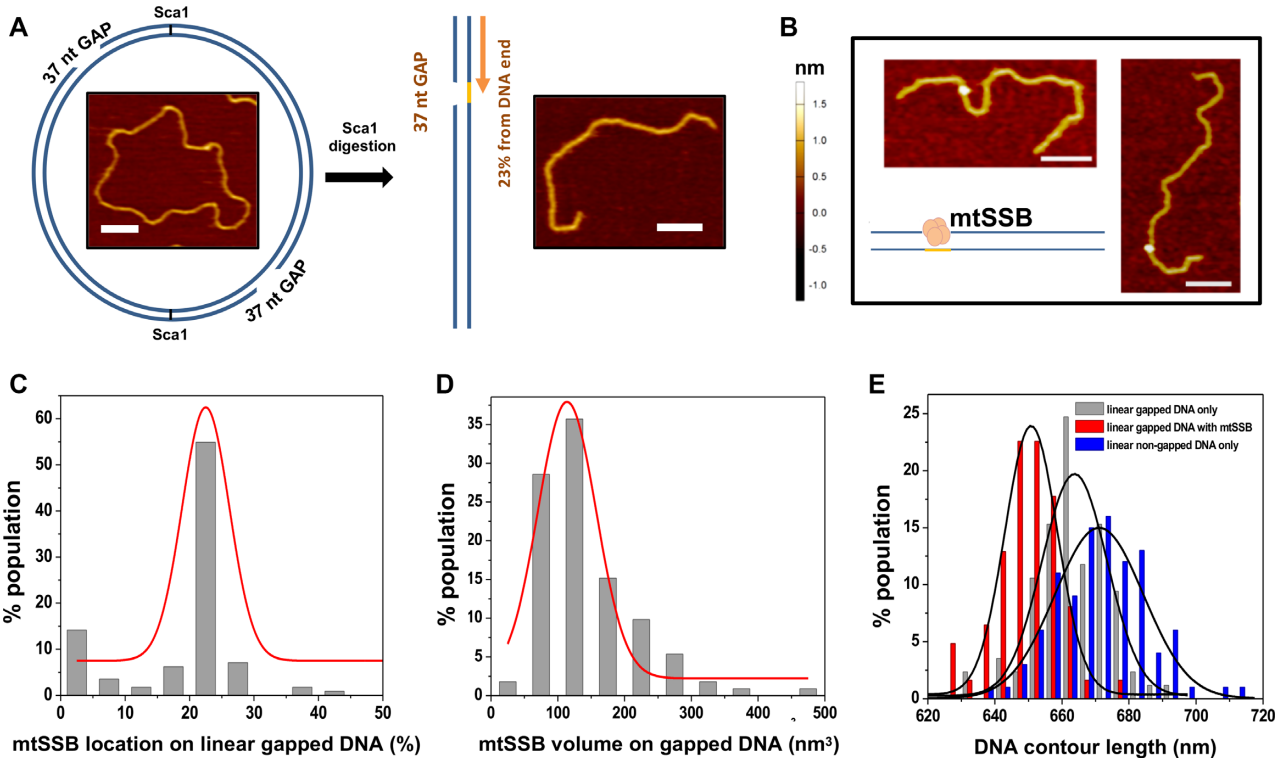

Figure 5. Binding of mtSSB tetramers to ssDNA gap shortens DNA lengths. (**A**) Cartoon representation of the process used to generate the circular and linear DNA substrate containing a 37-nt ssDNA gap, as described in 'Materials and Methods' section. Two inserts show AFM images of circular and linearized gapped DNA. X-Y scale bars = 100 nm. Circular plasmid DNA (4060 bp) contains a head-to-tail duplication, and digestion with Sca1 generates linear DNA fragments (2030 bp). (**B**) AFM images of mtSSB bound to linear gapped DNA. X-Y Scale bars = 50 nm. (**C**) The position distribution of mtSSB ($N = 113$) binding on the linear-gapped DNA was fit with a Gaussian function (red line, $R^2 = 0.92$), which is centered 22.6% (±4.6%) from the closer DNA end. (**D**) AFM volumes of mtSSB bound to the linear DNA substrate containing a 37-nt ssDNA gap ($N = 112$). The data were fit to a Gaussian function (red line, $R^2 = 0.91$) centered at 113.8 (±86.9) nm^3. (**E**) Lengths of linear DNA without treatment, after gapping procedures, and upon binding mtSSB. The data were fit to Gaussian functions ($R^2 > 0.91$) with peaks centered at 671.0 (±26.4) nm for non-gapped DNA alone (blue), 663.8 (±19.4) nm for gapped DNA alone (gray), and 650.8 (±15.7) nm for gapped DNA bound with mtSSB (red). All the samples were incubated in Incubation Buffer containing 20 mM HEPES (pH 7.5) and 100 mM NaCl and imaged in AFM Imaging Buffer containing 20 mM HEPES (pH 7.5), 100 mM NaCl, 10 mM $Mg(OAc)_2$ as described in 'Materials and Methods' section.

binding modes, we examined the conformation in mtSSB–ssDNA complexes at the single-molecule level. We applied a recently developed AFM imaging technique, DREEM, to monitor the surface electric potential difference across mtSSB–DNA complexes. Topographic and DREEM images are obtained simultaneously by mechanically vibrating the AFM cantilever near the fundamental resonance (ω_1), while applying a static voltage (V_{DC}) and a modulated bias voltage (V_{AC} at the first overtone ω_2) between the AFM cantilever and mica substrate. In DREEM imaging, both free proteins and DNA show a decrease in phase compared to the mica surface, but proteins show a greater contrast than DNA, which permits the identification of DNA paths in protein–DNA complexes (32–34,48).

The mtSSB–DNA complexes in DREEM phase images show dark regions corresponding to proteins and regions with decreased signal intensity corresponding to DNA (Figure 6A). DREEM amplitude images have contrast reversed and show the same features. DREEM images are reproducible at different scan angles, in trace and re-trace and through multiple scans. Tracing signal intensity identifies the path of DNA in mtSSB–ssDNA complexes, and the majority (92.5%, $N = 40$) of mtSSB-DNA complexes on the linear gapped DNA display a single DNA binding mode with only one DNA strand wrapping around a mtSSB tetramer. Cartoon models depicting ssDNA wrapping around a mtSSB tetramer are presented (Figure 6A). Importantly, the mtSSB–DNA complexes imaged using DREEM bound to a region centered 160.4 (±11.6) nm away from the DNA end (Figure 6B), consistent with the location of the 37-nt ssDNA gap on the linear DNA (Figure 5A). In contrast, recent DREEM images of ssDNA bound to nucleosomes clearly show a population of complexes with two ssDNA strands wrapping around histone octamers (48). Comparing images of ssDNA bound to mtSSB or to nucleosomes under the same DREEM imaging conditions supports our finding that DNA wraps mtSSB with one turn at the 37-nt ssDNA gap.

To test the possibility that the short length of the 37-nt gap may limit DNA wrapping to one turn, we also assessed binding of mtSSB to a circular double-stranded plasmid DNA containing a strand-specific 407-nt ssDNA gap (Figure 7A). AFM imaging revealed that binding by mtSSB was restricted to a single location on the gapped circular DNA (Figure 7B). As anticipated, the majority (92%, $N = 12$) of mtSSB–DNA complexes on the gapped circular

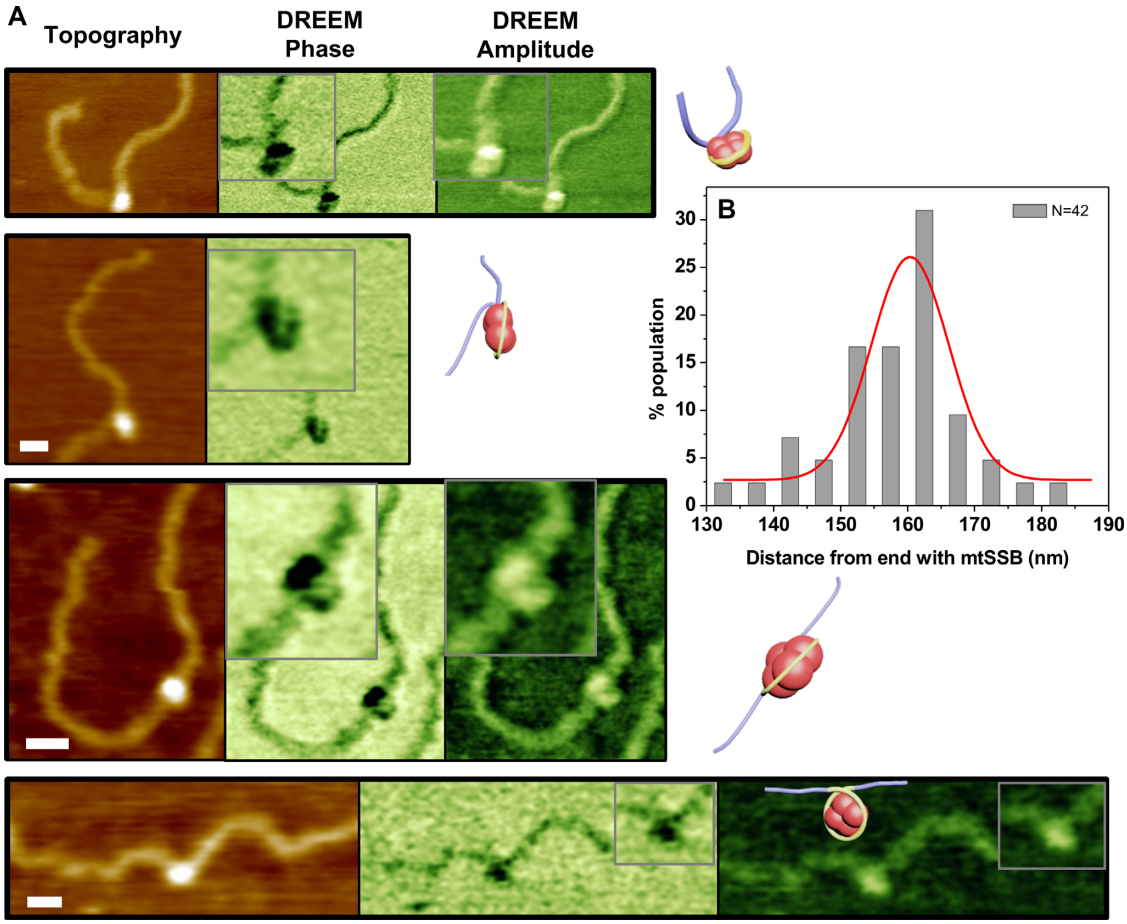

Figure 6. DREEM imaging of mtSSB on a linear DNA fragment containing a 37-nt ssDNA gap. (**A**) AFM topography (left panels), DREEM phase (middle panels) and DREEM amplitude (right panels) images of mtSSB interacting with the linear DNA substrate containing a 37-nt ssDNA gap. X-Y scale bar = 20 nm. The respective volumes of mtSSB–ssDNA complexes were measured as 147 nm^3 (top row), 192 nm^3 (second row) and 145 nm^3 (third row). DREEM-based cartoon models of mtSSB–DNA complexes depict mtSSB in red, the 37-nt ssDNA gap in green and flanking dsDNA arms in blue. In DREEM phase images, proteins and DNA show negative signals relative to the mica surface, but the proteins produce greater contrast (darker regions) compared to the DNA. (**B**) The distribution of distances between mtSSB and the closer DNA end in DREEM images. The data were fit to a Gaussian function (red line, $R^2 = 0.77$) centered at 160.4 ± 11.6 nm ($N = 42$). The ssDNA gap is located 470 bp (23%) from one end of the DNA fragment (2030 bp). All the samples were incubated in Incubation Buffer containing 20 mM HEPES (pH 7.5) and 100 mM NaCl at 37°C for 10 min and imaged in AFM Imaging Buffer containing 20 mM HEPES (pH 7.5), 100 mM NaCl, 10 mM $Mg(OAc)_2$, as described in 'Materials and Methods' section.

DNA displayed only one DNA strand wrapping around mtSSB protein in DREEM images (Figure 7C). However, the AFM volumes of mtSSB–DNA complexes were notably larger with the 407-nt-gapped DNA substrate (Figure 7C) than were observed with the 37-nt-gapped DNA substrate (Figure 6). Potential sources of additional AFM volume include the binding of longer ssDNA segments to each mtSSB tetramer and the binding of multiple mtSSB tetramers to each DNA molecule. Although the binding of additional ssDNA seems likely for some of the mtSSB–DNA complexes, we discount the more intricate winding paths for ssDNA on the surface of mtSSB proposed by Kang (30), because the multiple DNA wrappings needed to accommodate these models were not directly observed in DREEM images (Figure 7C). Binding mixtures for this substrate were assembled with a higher protein/DNA ratio to enable visualization of multiple individual mtSSB–DNA complexes within the same gapped region (see 'Materials and Methods' section), which could have increased the binding density of mtSSB. Because discrete mtSSB tetramers were not resolved in all images of mtSSB–DNA complexes, we cannot discount the possibility of two mtSSB tetramers binding within a single 407-nt ssDNA gap.

To resolve this ambiguity, we utilized DREEM imaging to assess binding and wrapping of ssDNA with an intermediate length by mtSSB and *E. coli* SSB. When mtSSB was incubated with a defined 90-nt oligonucleotide under identical solution conditions, the predominant configuration of mtSSB–DNA complexes (85%, $N = 59$) showed one strand of ssDNA wrapping around the mtSSB tetramer (Figure 8A), whereas a small subpopulation of mtSSB–DNA complexes (15%) showed two strands of ssDNA wrapping around the protein (Figure 8B). Instances of two mtSSB tetramers binding to a single 90-nt oligomer were not detected at this binding density (0.5 mtSSB/90mer), although other investigators have observed double binding of mtSSB to oligo$(dT)_{60}$ by EMSA with super-stoichiometric binding densities and similar solution conditions (31). DREEM

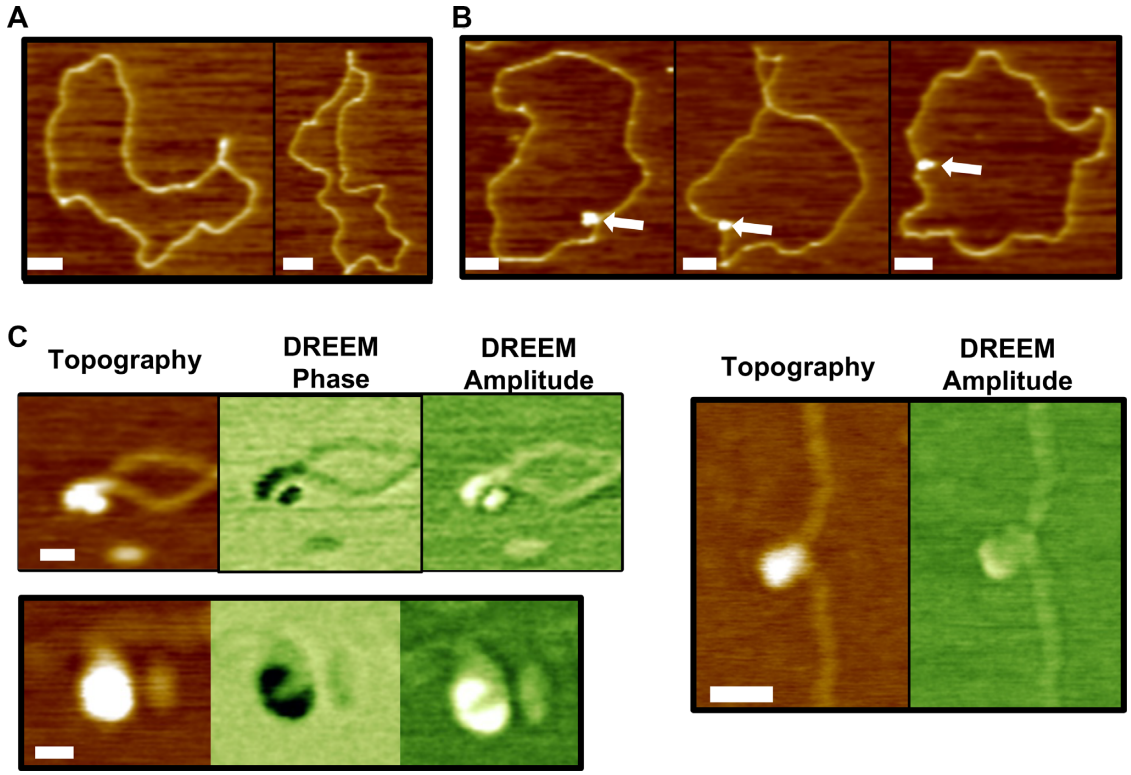

Figure 7. AFM and DREEM imaging of mtSSB on a circular DNA substrate containing a 407-nt ssDNA gap. AFM topography images of circular plasmid DNA containing a 407-nt ssDNA gap in the (**A**) absence and (**B**) presence of mtSSB (white arrows). X-Y scale bar = 100 nm. (**C**) AFM topography (left panels), DREEM phase (middle panels) and DREEM amplitude (right panels) images of mtSSB interacting with circular DNA containing a 407-nt ssDNA gap. The volume of mtSSB on DNA with a 407-nt ssDNA gap was measured as 246 nm^3 (top left panels), 466 nm^3 (bottom left panels) and 368 nm^3 (right panel). X-Y scale bar = 20 nm. Samples were prepared for AFM and DREEM in Incubation Buffer containing 20 mM HEPES (pH 7.5) and 100 mM NaCl at 37°C for 10 min and imaged in AFM Imaging Buffer containing 20 mM HEPES (pH 7.5), 100 mM NaCl, 10 mM $Mg(OAc)_2$ as described in 'Materials and Methods' section.

imaging also revealed mixed modes for wrapping the 90-nt oligonucleotide around the *E. coli* SSB. Only 35% of *E. coli* SSB–DNA complexes ($N = 60$) displayed one strand of ssDNA wrapping around the *E. coli* SSB tetramer (Figure 9A), whereas 65% of complexes showed two strands of ssDNA wrapping around the protein (Figure 9B). Complexes with multiple *E. coli* SSB tetramers bound to a single 90-nt oligomer were not detected. The presence of a mixed population of wrapping modes for protein–DNA complexes is not surprising. For example, crystallography shows that nucleosome core particles are wrapped by 1.67 left-handed superhelical turns of 147 bp of dsDNA (63,64), and DREEM images reveal either one or two bound strands of double-stranded DNA, depending on the orientation of the nucleosomes on the mica surface (32,48). ssDNA also wraps around recombinant histone octamers in two populations with either one or two strands of ssDNA visible in DREEM images (48). The distribution of mtSSB–DNA and *E. coli* SSB–DNA complexes into single- and double-wrapped populations may be influenced by incidental structural factors, such as the acidic C-terminal tail of *E. coli* SSB possibly affecting the orientation of the protein–DNA complex upon binding mica. The relative abundance of single-wrapped and double-wrapped species, as well as potential interconversion between the forms, may depend on solution conditions such as Mg^{2+} ion and salt concentration. Nevertheless, the differential presentation at 100 mM NaCl of mtSSB–DNA with mainly single DNA wraps and *E. coli* SSB–DNA with mainly double DNA wraps is intriguing. Also, cross-sectional analysis of DREEM images reveals different spacing of DNA on the two proteins. The edge-to-edge distances for *one* strand of ssDNA wrapped around mtSSB (5.1 ± 1.1 nm, mean ± SD, $N = 50$) and *E. coli* SSB (5.2 ± 1.3 nm, $N = 21$) were comparable (Figures 8C and 9C, respectively). However, the edge-to-edge distance for *two* strands of ssDNA around mtSSB (11.1 ± 2.4 nm, $N = 9$) was significantly ($P < 0.05$) wider than what was observed for *E. coli* SSB (7.5 ± 1.9 nm, $N = 39$). This difference suggests that mtSSB–DNA complexes may be structurally distinct from the more tightly wrapped *E. coli* SSB-DNA complexes. The crystal structure of a chymotryptic fragment of *E. coli* SSB bound to two $(dC)_{35}$ molecules (PDB ID: 1EYG) reveals extensive wrapping of ssDNA on the surface of the SSB tetramer (65). Availability of a crystal structure for human mtSSB bound to ssDNA will help to determine whether the wider separation of 90-nt ssDNA strands seen in DREEM images (Figure 8) are caused by random positioning of excess length during sample deposition or by specific protein–DNA interactions.

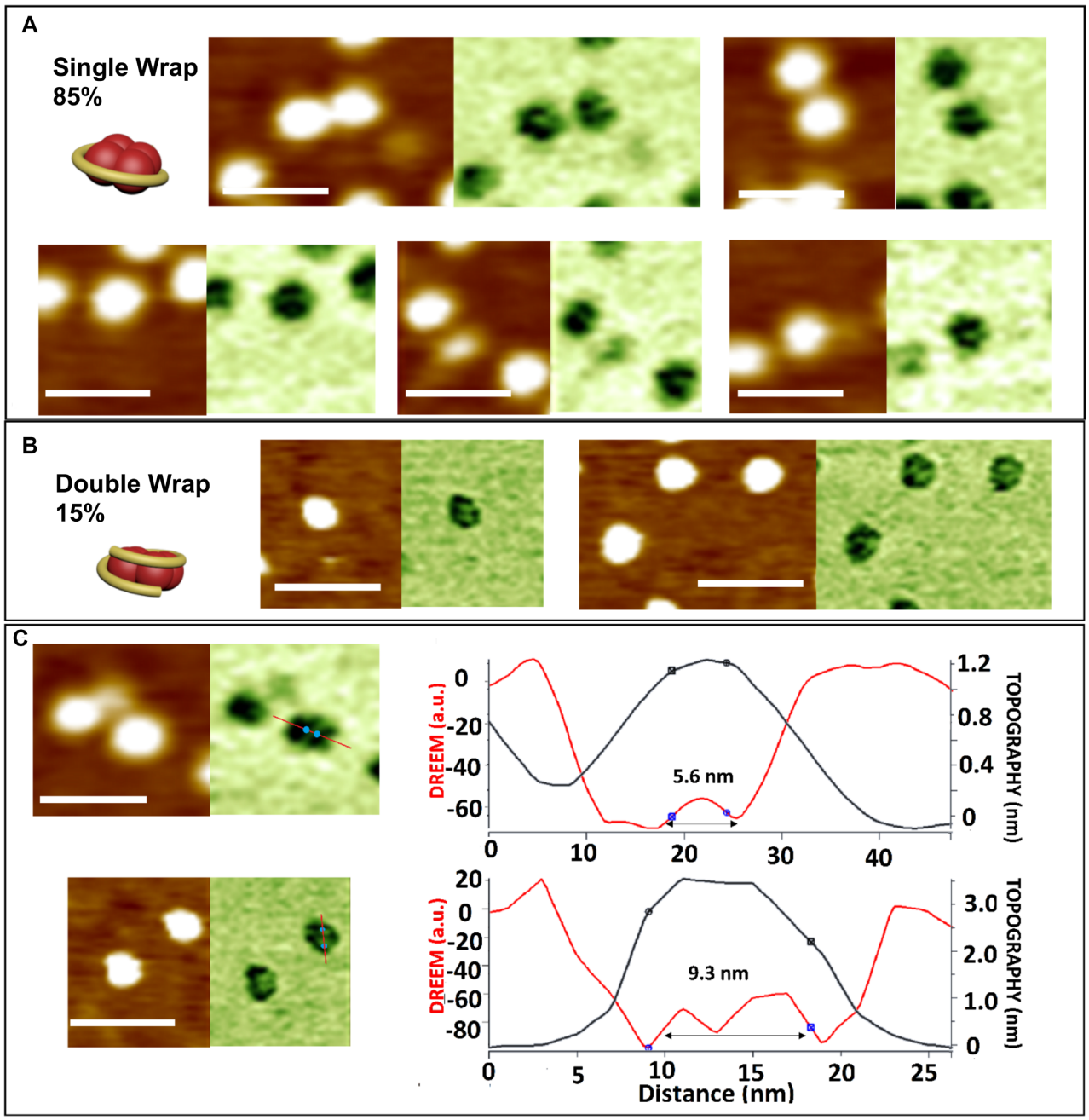

Figure 8. DREEM imaging shows wrapping paths of a 90-nt ssDNA oligomer around mtSSB. Samples containing 80 nM mtSSB and 159 nM 90-nt ssDNA were incubated for 10 min at 37°C in Incubation Buffer containing 20 mM HEPES (pH 7.5) and 100 mM NaCl and imaged in AFM Imaging Buffer containing 20 mM HEPES (pH 7.5), 100 mM NaCl, 10 mM $Mg(OAc)_2$ as described in 'Materials and Methods' section. AFM topography (left panels) and DREEM phase (right panels) images of mtSSB ($N = 59$) show (**A**) one strand (85%) or (**B**) two strands (15%) of ssDNA crossing the face of the mtSSB tetramer. DREEM-based cartoon models of mtSSB–DNA complexes depict mtSSB in red and the 90-nt ssDNA in yellow. (**C**) Cross-sectional analysis of the edge-to-edge distance for one strand (top panel) or two strands (bottom panel) of ssDNA. DNA edges are identified at half maxima of the DNA DREEM signal (blue circles). X-Y scale bar = 25 nm.

DISCUSSION

SSB proteins are ubiquitous in nature and exhibit an assortment of different oligomeric structures and interactions with other proteins (66). The *E. coli* SSB is the bacterial prototype, and it shares significant sequence and structural homology with mtSSB. *Escherichia coli* SSB is a stable homotetramer composed of four 19 kDa monomers, each with an N-terminal oligonucleotide binding domain and an intrinsically disordered linker (IDL) region terminating in an unstructured C-terminal tail (66). ssDNA winds around *E. coli* SSB tetramers at low protein/DNA ratios (57,67,68), and ssDNA contacts all four subunits when the tetrameric core is fully wrapped by 65 nt in the $(SSB)_{65}$ binding mode (56,65). Binding ssDNA in the $(SSB)_{65}$ mode is not highly

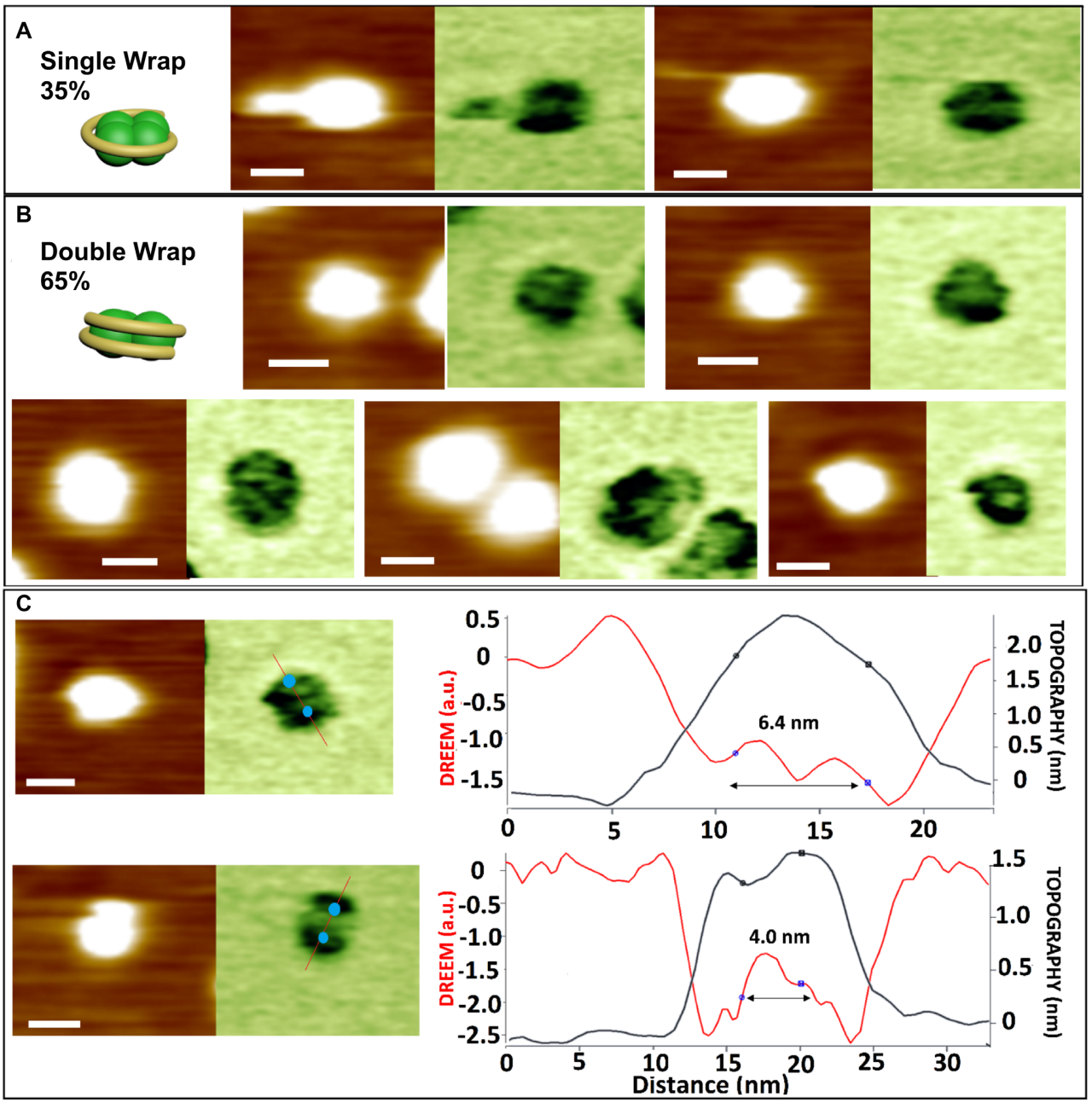

Figure 9. DREEM imaging shows wrapping paths of a 90-nt ssDNA oligomer around *Escherichia coli* SSB. Samples containing 80 nM *E. coli* SSB and 159 nM 90-nt ssDNA were incubated for 10 min at 37°C in Incubation Buffer containing 20 mM HEPES (pH 7.5) and 100 mM NaCl and imaged in AFM Imaging Buffer containing 20 mM HEPES (pH 7.5), 100 mM NaCl, 10 mM $Mg(OAc)_2$ as described in 'Materials and Methods' section. AFM topography (left panels) and DREEM phase (right panels) images of *E. coli* SSB ($N = 60$) show (**A**) one strand (35%) or (**B**) two strands (65%) of ssDNA crossing the face of the *E. coli* tetramer. DREEM-based cartoon models of *E. coli* SSB–DNA complexes depict *E. coli* SSB in green and the 90-nt ssDNA in yellow. (**C**) Cross-sectional analysis of the edge-to-edge distance for two strands (top panel) or one strand (bottom panel) of ssDNA. DNA edges are identified at half maxima of the DNA DREEM signal (blue circles). X-Y Scale bar = 10 nm.

cooperative (55), and the $(SSB)_{65}$ binding mode is thought to facilitate diffusion along ssDNA (69,70). *Escherichia coli* SSB also adopts a highly cooperative $(SSB)_{35}$ DNA binding mode in which only two subunits make direct contact with 35 nt of ssDNA (65,66). The crystal structure of *E. coli* SSB bound to two $(dC)_{35}$ molecules suggests a structural basis for the different binding modes (65). Many factors contribute to the transition between these two DNA binding modes. Transitions can be modulated *in vitro* by altering protein/DNA ratios and the concentration of mono- and multi-valent cations (56,68), and negative cooperativity among the subunits within an individual *E. coli* SSB tetramer contributes to the transition between the $(SSB)_{35}$ and $(SSB)_{65}$ DNA binding modes (71). The C-terminal tail is required to effect rapid transitions between the two major binding modes of *E. coli* SSB (72), and the length and con-

formation of the IDL between the oligonucleotide binding domain and the C-terminal portion of SSBs have recently been proposed to modulate cooperative binding to ssDNA (73).

Early electron micrographs showed a random distribution of mtSSB tetramers bound to individual strands of poly(dT), which suggested low cooperativity of DNA binding for mtSSB (37). Mikhailov and Bogenhagen also obtained hints that mtSSB did not bind DNA cooperatively *in vitro* when they demonstrated that oligo$(dT)_{80}$ binds two tetramers of *X. laevis* mtSSB or *E. coli* SSB *in vitro*, and that heterologous double complexes are created by random selection of SSB tetramers from mixtures of *X. laevis* mtSSB and *E. coli* SSB. The absence of a preference for binding either two *X. laevis* mtSSB tetramers or two *E. coli* SSB tetramers implies no cooperative advantage for binding the second tetramer to oligo$(dT)_{80}$ (27). In our study, we utilized AFM and DREEM imaging to compare binding of *E. coli* SSB and human mtSSB to a variety of DNA substrates. AFM imaging revealed a random DNA binding pattern for human mtSSB bound to M13mp18 ssDNA over a range of protein/DNA ratios (Figure 3). *Escherichia coli* SSB exhibited a similarly random binding pattern, although a minor fraction of molecules formed nucleoprotein filaments with M13mp18 ssDNA at physiological salt concentrations (Figure 4). Both proteins formed these structures more readily at 20 mM NaCl (Supplementary Figures S4 and 5), but the higher incidence and greater length of *E. coli* SSB-M13mp18 DNA filaments suggests additional factors are affecting cooperative DNA binding of these proteins. Comparing the crystal structures of *E. coli* SSB and human mtSSB revealed a common core structure but also suggested that cross-species heterotetramers cannot form due to crucial differences in the dimer-dimer interface (74). Also, human mtSSB does not exhibit negative inter-subunit cooperativity that is essential for *E. coli* SSB to transition to a highly cooperative DNA binding mode (31). Human mtSSB lacks the acidic C-terminal tail that is present *in E. coli* SSB, but it contains two stretches (residues 1–9 and 55–59) that are disordered in the mtSSB crystal structure and missing in *E. coli* SSB (15,30). The notion that the C-terminal tail of *E. coli* SSB regulates cooperative binding to ssDNA (73) raises the obvious possibility that the absence of the C-terminal tail in mtSSB may help to explain the lack of highly cooperative DNA binding. Collectively, these studies support our observations that mtSSB does not bind ssDNA in a highly cooperative fashion.

Understanding the roles and interactions of mtSSB with binding partners at the mtDNA replication fork is essential to understanding the mechanisms governing maintenance of the mitochondrial genome. The crystal structure of full-length *E. coli* SSB reveals that the disordered C-terminal domain extends laterally away from the DNA-binding domains (75), and this C-terminal acidic tail is known to facilitate recruitment of protein binding partners *in vivo* (69,72,76). For example, the C-terminal tails in $(SSB)_{65}$ binding mode stimulate RecA filament elongation reactions (69,70). Extending similar logic, the absence of a homologous C-terminal tail in mtSSB predicts limited opportunities for mtDNA replication to include certain recombination and repair pathways seen in the *E. coli* system. A recent report described the kinetics and thermodynamics of human mtSSB binding to ssDNA (31). Similar to *E. coli* SSB, mtSSB exhibits rapid, high-affinity binding to dT_{30} and dT_{60} homo-oligomers, and equilibrium titration experiments suggested the DNA binding site size is modulated by Mg^{2+} ion and NaCl concentrations. Although their data support a single DNA binding step, measurements at extreme mtSSB/dT_{60} and dT_{60}/mtSSB ratios in the presence and absence of Mg^{2+} ions permitted refinement of their kinetic scheme to include a transient complex of mtSSB and frayed oligo$(dT)_{60}$. This intermediate can disassociate or rapidly progress to a more fully wrapped state, or mtSSB can switch directly to a second molecule of dT_{60} without dissociation. In this model the wrapping reaction is slightly favored, and isomerization increases the population of complexes in the mtSSB-partially frayed dT_{60} state, which may facilitate sliding and strand transfer by mtSSB (31). Another recent report described use of an optical tweezer instrument to characterize the elastic and energetic properties of mtSSB binding to pre-existing stretches of ssDNA and to ssDNA intermediates generated during DNA synthesis *in vitro* (77). Two DNA binding modes (low and high site sizes) are exhibited when mtSSB binds pre-formed ssDNA molecules under tension, and site-size is modulated by the concentration of mtSSB and NaCl. However, only the smaller site-size binding mode (34–54 nt/tetramer) is evident when binding ssDNA generated during DNA synthesis at ∼30 nt/s by bacteriophage Phi29 DNA polymerase-helicase. The authors conclude that unidirectional, gradual release of ssDNA during DNA synthesis is key to determining the DNA wrapping mode of mtSSB along nascent ssDNA, and they suggest that proper selection of the binding mode is crucial to facilitate subsequent DNA transactions *in vivo*.

We wish to compare the SSB proteins of human mitochondria and the plastid-like organelle of the malaria protozoan *Plasmodium falciparum*. *P. falciparum* possesses a single, essential apicoplast organelle that contains an ∼35 kb covalently-closed circular DNA genome (78). Among the nuclear-encoded proteins that are transported into the organelle to maintain apicoplast DNA is a homotetrameric *P. falciparum* SSB (*Pf*-SSB) (79,80). *Pf*-SSB is structurally similar and highly homologous to *E. coli* SSB, and it also possesses an unstructured, acidic C-terminal tail that may facilitate interactions with other DNA metabolizing enzymes (80). The crystal structure of *Pf*-SSB bound to two $(dT)_{35}$ molecules indicates that ssDNA wraps completely around the tetramer, similar to the topology of the *E. coli* $(SSB)_{65}$ binding mode, but the polarity of bound DNA and the specific amino acid contacts are different than observed in the *E. coli* SSB structure (80). In addition, DNA binding by *Pf*-SSB is not highly cooperative, and *Pf*-SSB exhibits only a single DNA binding mode with ssDNA fully contacting all four subunits and a binding site size of 52–65 nt/tetramer (81). *Pf*-SSB does not transition to a highly cooperative $(SSB)_{35}$ DNA binding mode seen in *E. coli* SSB, and it does not exhibit negative intra-tetramer cooperativity for binding a second $(dT)_{35}$ molecule (81). Loss of a tetramer-tetramer interface in neighboring unit cells of the *Pf*-SSB protein crystals may be consistent with this failure to transition to a more cooperative DNA binding mode

(80). Lohman and co-workers suggest these basic differences between *Pf*-SSB and *E. coli* SSB may reflect specific functions of *Pf*-SSB in the apicoplast (81). Given the functional similarities of *Pf*-SSB and mtSSB and the common organellar niche, we speculate that *Pf*-SSB may be more similar to mtSSB than to *E. coli* SSB. Future efforts to visualize ssDNA wrapping around *Pf*-SSB tetramers by AFM and DREEM would inform this comparison.

The distributive binding of ssDNA by mtSSB carries implications for the maintenance of mtDNA. Falkenberg and co-workers performed ChIP-seq with antibodies specific for human mtSSB to determine the *in vivo* occupancy of mtSSB along the mitochondrial genome of isolated HeLa cell mitochondria (82). Analysis of recovered ssDNA by strand-specific next generation sequencing revealed a striking strand bias with mtSSB predominantly bound to the parental heavy strand, which is displaced during the strand displacement mode of mtDNA synthesis. Strand-specific occupancy of the heavy strand in a gradient from a position just downstream from the D-loop and extending to OriL strongly supports the strand displacement model of mtDNA replication (83). The natural abundance of mtSSB in cultured HeLa cells should be sufficient to saturate the mitochondrial genome *in vivo* (82,84), however ChIP-seq with antibodies against mtSSB cannot differentiate complete or incomplete occupancy of displaced ssDNA by mtSSB. Any resulting gaps distributed along the displaced heavy strand would be subject to forming secondary structures that could promote mtDNA deletions driven by primer relocation events. In fact, addition of *E. coli* SSB helps to minimize deletion mutagenesis artifacts during *Taq* DNA polymerase chain reactions *in vitro*, and explanations for this effect explicitly include the ability of SSB to melt template secondary structure and to prevent inappropriate primer relocation events (85). Given that mtDNA deletions predominantly occur within the zone of the displaced heavy strand (86–88), we hypothesize that non-cooperative DNA binding by mtSSB fosters deletion mutagenesis in human mtDNA during strand displacement mtDNA replication *in vivo*. Relatedly, incomplete occupancy of single-stranded mtDNA intermediates because of distributed binding by mtSSB would leave the mitochondrial genome vulnerable to chemical mutagenesis or even destruction due to persistent strand breaks.

SUPPLEMENTARY DATA

Supplementary Data are available at NAR Online.

ACKNOWLEDGEMENTS

We wish to thank Drs Sara Andres and Carl Anderson at the NIEHS for critical evaluation of the manuscript. We thank Dr Harvey Sage (Duke University) for assistance with analytical ultracentrifugation, and Dr Katarzyna Bebenek (NIEHS) for providing plasmid DNA containing the long single-stranded gap.

FUNDING

Intramural Research Program of the NIH, National Institute of Environmental Health Sciences [ES065078 to W.C.C.]; Extramural Research Program of the NIH [P30ES025128 to P.K., R01GM107559, R01GM123246, R21ES027641 to H.W.]. Funding for open access charge: National Institute of Environmental Health Sciences, NIH [ES 065078].
Conflict of interest statement. None declared.

REFERENCES

1. Chase,J.W. and Williams,K.R. (1986) Single-stranded DNA binding proteins required for DNA replication. *Annu. Rev. Biochem.*, **55**, 103–136.
2. Pestryakov,P.E. and Lavrik,O.I. (2008) Mechanisms of single-stranded DNA-binding protein functioning in cellular DNA metabolism. *Biochemistry (Mosc)*, **73**, 1388–1404.
3. Ashton,N.W., Bolderson,E., Cubeddu,L., O'Byrne,K.J. and Richard,D.J. (2013) Human single-stranded DNA binding proteins are essential for maintaining genomic stability. *BMC Mol. Biol.*, **14**, 9.
4. Antony,E., Weiland,E., Yuan,Q., Manhart,C.M., Nguyen,B., Kozlov,A.G., McHenry,C.S. and Lohman,T.M. (2013) Multiple C-terminal tails within a single E. coli SSB homotetramer coordinate DNA replication and repair. *J. Mol. Biol.*, **425**, 4802–4819.
5. Bianco,P.R. (2017) The tale of SSB. *Prog. Biophys. Mol. Biol.*, **127**, 111–118.
6. Richard,D.J., Bolderson,E. and Khanna,K.K. (2009) Multiple human single-stranded DNA binding proteins function in genome maintenance: structural, biochemical and functional analysis. *Crit. Rev. Biochem. Mol. Biol.*, **44**, 98–116.
7. Dickey,T.H., Altschuler,S.E. and Wuttke,D.S. (2013) Single-stranded DNA-binding proteins: multiple domains for multiple functions. *Structure*, **21**, 1074–1084.
8. Anderson,S., Bankier,A.T., Barrell,B.G., de Bruijn,M.H., Coulson,A.R., Drouin,J., Eperon,I.C., Nierlich,D.P., Roe,B.A., Sanger,F. *et al.* (1981) Sequence and organization of the human mitochondrial genome. *Nature*, **290**, 457–465.
9. DeBalsi,K.L., Hoff,K.E. and Copeland,W.C. (2017) Role of the mitochondrial DNA replication machinery in mitochondrial DNA mutagenesis, aging and age-related diseases. *Ageing Res. Rev.*, **33**, 89–104.
10. Copeland,W.C. (2008) Inherited mitochondrial diseases of DNA replication. *Annu. Rev. Med.*, **59**, 131–146.
11. Ciesielski,G.L., Oliveira,M.T. and Kaguni,L.S. (2016) Animal mitochondrial DNA replication. *Enzymes*, **39**, 255–292.
12. Barat,M. and Mignotte,B. (1981) A DNA binding protein from Xenopus laevis oocyte mitochondria. *Chromosoma*, **82**, 583–593.
13. Van Tuyle,G.C. and Pavco,P.A. (1985) The rat liver mitochondrial DNA-protein complex: displaced single strands of replicative intermediates are protein coated. *J. Cell Biol.*, **100**, 251–257.
14. Tiranti,V., Barat-Gueride,B., Bijl,J., DiDonato,S. and Zeviani,M. (1991) A full-length cDNA encoding a mitochondrial DNA-specific single-stranded DNA binding protein from Xenopus laevis. *Nucleic Acids Res.*, **19**, 4291.
15. Tiranti,V., Rocchi,M., DiDonato,S. and Zeviani,M. (1993) Cloning of human and rat cDNAs encoding the mitochondrial single-stranded DNA-binding protein (SSB). *Gene*, **126**, 219–225.
16. Van Dyck,E., Foury,F., Stillman,B. and Brill,S.J. (1992) A single-stranded DNA binding protein required for mitochondrial DNA replication in S. cerevisiae is homologous to E. coli SSB. *EMBO J.*, **11**, 3421–3430.
17. Maier,D., Farr,C.L., Poeck,B., Alahari,A., Vogel,M., Fischer,S., Kaguni,L.S. and Schneuwly,S. (2001) Mitochondrial single-stranded DNA-binding protein is required for mitochondrial DNA replication and development in Drosophila melanogaster. *Mol. Biol. Cell*, **12**, 821–830.
18. Farr,C.L., Matsushima,Y., Lagina,A.T. 3rd, Luo,N. and Kaguni,L.S. (2004) Physiological and biochemical defects in functional interactions of mitochondrial DNA polymerase and DNA-binding mutants of single-stranded DNA-binding protein. *J. Biol. Chem.*, **279**, 17047–17053.
19. Ruhanen,H., Borrie,S., Szabadkai,G., Tyynismaa,H., Jones,A.W., Kang,D., Taanman,J.W. and Yasukawa,T. (2010) Mitochondrial single-stranded DNA binding protein is required for maintenance of

mitochondrial DNA and 7S DNA but is not required for mitochondrial nucleoid organisation. *Biochim. Biophys. Acta*, **1803**, 931–939.
20. Genuario,R. and Wong,T.W. (1993) Stimulation of DNA polymerase gamma by a mitochondrial single-strand DNA binding protein. *Cell Mol. Biol. Res.*, **39**, 625–634.
21. Oliveira,M.T. and Kaguni,L.S. (2011) Reduced stimulation of recombinant DNA polymerase gamma and mitochondrial DNA (mtDNA) helicase by variants of mitochondrial single-stranded DNA-binding protein (mtSSB) correlates with defects in mtDNA replication in animal cells. *J. Biol. Chem.*, **286**, 40649–40658.
22. Williams,A.J. and Kaguni,L.S. (1995) Stimulation of Drosophila mitochondrial DNA polymerase by single-stranded DNA-binding protein. *J. Biol. Chem.*, **270**, 860–865.
23. Farr,C.L., Wang,Y. and Kaguni,L.S. (1999) Functional interactions of mitochondrial DNA polymerase and single-stranded DNA-binding protein. Template-primer DNA binding and initiation and elongation of DNA strand synthesis. *J. Biol. Chem.*, **274**, 14779–14785.
24. Ciesielski,G.L., Bermek,O., Rosado-Ruiz,F.A., Hovde,S.L., Neitzke,O.J., Griffith,J.D. and Kaguni,L.S. (2015) Mitochondrial Single-stranded DNA-binding proteins stimulate the activity of DNA polymerase gamma by organization of the template DNA. *J. Biol. Chem.*, **290**, 28697–28707.
25. Korhonen,J.A., Gaspari,M. and Falkenberg,M. (2003) TWINKLE Has 5′ → 3′ DNA helicase activity and is specifically stimulated by mitochondrial single-stranded DNA-binding protein. *J. Biol. Chem.*, **278**, 48627–48632.
26. Korhonen,J.A., Pham,X.H., Pellegrini,M. and Falkenberg,M. (2004) Reconstitution of a minimal mtDNA replisome in vitro. *EMBO J.*, **23**, 2423–2429.
27. Mikhailov,V.S. and Bogenhagen,D.F. (1996) Effects of Xenopus laevis mitochondrial single-stranded DNA-binding protein on primer-template binding and 3′→5′ exonuclease activity of DNA polymerase gamma. *J. Biol. Chem.*, **271**, 18939–18946.
28. Ghosh,S., Hamdan,S.M. and Richardson,C.C. (2010) Two modes of interaction of the single-stranded DNA-binding protein of bacteriophage T7 with the DNA polymerase-thioredoxin complex. *J. Biol. Chem.*, **285**, 18103–18112.
29. Sharma,N., Chakravarthy,S., Longley,M.J., Copeland,W.C. and Prakash,A. (2018) The C-terminal tail of the NEIL1 DNA glycosylase interacts with the human mitochondrial single-stranded DNA binding protein. *DNA Repair (Amst.)*, **65**, 11–19.
30. Yang,C., Curth,U., Urbanke,C. and Kang,C. (1997) Crystal structure of human mitochondrial single-stranded DNA binding protein at 2.4 A resolution. *Nat. Struct. Biol.*, **4**, 153–157.
31. Qian,Y. and Johnson,K.A. (2017) The human mitochondrial single-stranded DNA-binding protein displays distinct kinetics and thermodynamics of DNA binding and exchange. *J. Biol. Chem.*, **292**, 13068–13084.
32. Wu,D., Kaur,P., Li,Z.M., Bradford,K.C., Wang,H. and Erie,D.A. (2016) Visualizing the path of DNA through proteins using DREEM imaging. *Mol. Cell*, **61**, 315–323.
33. Benarroch-Popivker,D., Pisano,S., Mendez-Bermudez,A., Lototska,L., Kaur,P., Bauwens,S., Djerbi,N., Latrick,C.M., Fraisier,V., Pei,B. *et al.* (2016) TRF2-Mediated control of telomere DNA topology as a mechanism for Chromosome-End protection. *Mol. Cell*, **61**, 274–286.
34. Kaur,P., Wu,D., Lin,J., Countryman,P., Bradford,K.C., Erie,D.A., Riehn,R., Opresko,P.L. and Wang,H. (2016) Enhanced electrostatic force microscopy reveals higher-order DNA looping mediated by the telomeric protein TRF2. *Sci. Rep.*, **6**, 20513.
35. Longley,M.J., Smith,L.A. and Copeland,W.C. (2009) Preparation of human mitochondrial single-stranded DNA-binding protein. *Methods Mol. Biol.*, **554**, 73–85.
36. Gill,S.C. and von Hippel,P.H. (1989) Calculation of protein extinction coefficients from amino acid sequence data. *Anal. Biochem.*, **182**, 319–326.
37. Curth,U., Urbanke,C., Greipel,J., Gerberding,H., Tiranti,V. and Zeviani,M. (1994) Single-stranded-DNA-binding proteins from human mitochondria and Escherichia coli have analogous physicochemical properties. *Eur. J. Biochem.*, **221**, 435–443.
38. Sambrook,J., Fritsch,E.F. and Maniatis,T. (1989) *Molecular Cloning, A Laboratory Manual*. 2nd edn. Cold Spring Harbor Laboratory Press, NY.
39. Geng,H., Du,C., Chen,S., Salerno,V., Manfredi,C. and Hsieh,P. (2011) In vitro studies of DNA mismatch repair proteins. *Anal. Biochem.*, **413**, 179–184.
40. Buechner,C.N. and Tessmer,I. (2013) DNA substrate preparation for atomic force microscopy studies of protein-DNA interactions. *J. Mol. Recognit.*, **26**, 605–617.
41. Countryman,P., Fan,Y., Gorthi,A., Pan,H., Strickland,J., Kaur,P., Wang,X., Lin,J., Lei,X., White,C. *et al.* (2018) Cohesin SA2 is a sequence-independent DNA-binding protein that recognizes DNA replication and repair intermediates. *J. Biol. Chem.*, **293**, 1054–1069.
42. Bebenek,K. and Kunkel,T.A. (1995) Analyzing fidelity of DNA polymerases. *Methods Enzymol.*, **262**, 217–232.
43. Heyduk,T., Ma,Y., Tang,H. and Ebright,R.H. (1996) Fluorescence anisotropy: rapid, quantitative assay for protein-DNA and protein-protein interaction. *Methods Enzymol.*, **274**, 492–503.
44. Heyduk,T. and Lee,J.C. (1990) Application of fluorescence energy transfer and polarization to monitor Escherichia coli cAMP receptor protein and lac promoter interaction. *Proc. Natl. Acad. Sci. U.S.A.*, **87**, 1744–1748.
45. Cornish-Bowden,A. (2004) *Fundamentals of Enzyme Kinetics*. 3rd edn. Portland Press Ltd.
46. Poklar,N., Lah,J., Salobir,M., Macek,P. and Vesnaver,G. (1997) pH and temperature-induced molten globule-like denatured states of equinatoxin II: a study by UV-melting, DSC, far- and near-UV CD spectroscopy, and ANS fluorescence. *Biochemistry*, **36**, 14345–14352.
47. Niesen,F.H., Berglund,H. and Vedadi,M. (2007) The use of differential scanning fluorimetry to detect ligand interactions that promote protein stability. *Nat. Protoc.*, **2**, 2212–2221.
48. Adkins,N.L., Swygert,S.G., Kaur,P., Niu,H., Grigoryev,S.A., Sung,P., Wang,H. and Peterson,C.L. (2017) Nucleosome-like, Single-stranded DNA (ssDNA)-Histone octamer complexes and the implication for DNA double strand break repair. *J. Biol. Chem.*, **292**, 5271–5281.
49. Mahoungou,C., Ghrir,R., Lecaer,J.P., Mignotte,B. and Baratgueride,M. (1988) The Amino-Terminal sequence of the Xenopus-Laevis mitochondrial Ssb is homologous to that of the Escherichia-Coli protein. *FEBS Lett.*, **235**, 267–270.
50. Thommes,P., Farr,C.L., Marton,R.F., Kaguni,L.S. and Cotterill,S. (1995) Mitochondrial single-stranded DNA-binding protein from Drosophila embryos. Physical and biochemical characterization. *J. Biol. Chem.*, **270**, 21137–21143.
51. Li,K. and Williams,R.S. (1997) Tetramerization and single-stranded DNA binding properties of native and mutated forms of murine mitochondrial single-stranded DNA-binding proteins. *J. Biol. Chem.*, **272**, 8686–8694.
52. Stroumbakis,N.D., Li,Z. and Tolias,P.P. (1994) RNA- and single-stranded DNA-binding (SSB) proteins expressed during Drosophila melanogaster oogenesis: a homolog of bacterial and eukaryotic mitochondrial SSBs. *Gene*, **143**, 171–177.
53. Krauss,G., Sindermann,H., Schomburg,U. and Maass,G. (1981) Escherichia coli single-strand deoxyribonucleic acid binding protein: stability, specificity, and kinetics of complexes with oligonucleotides and deoxyribonucleic acid. *Biochemistry*, **20**, 5346–5352.
54. Robberson,D.L. and Clayton,D.A. (1972) Replication of mitochondrial DNA in mouse L cells and their thymidine kinase - derivatives: displacement replication on a covalently-closed circular template. *Proc. Natl. Acad. Sci. U.S.A.*, **69**, 3810–3814.
55. Lohman,T.M., Overman,L.B. and Datta,S. (1986) Salt-dependent changes in the DNA binding co-operativity of Escherichia coli single strand binding protein. *J. Mol. Biol.*, **187**, 603–615.
56. Lohman,T.M. and Overman,L.B. (1985) Two binding modes in Escherichia coli single strand binding protein-single stranded DNA complexes. Modulation by NaCl concentration. *J. Biol. Chem.*, **260**, 3594–3603.
57. Griffith,J.D., Harris,L.D. and Register,J. 3rd (1984) Visualization of SSB-ssDNA complexes active in the assembly of stable RecA-DNA filaments. *Cold Spring Harb. Symp. Quant. Biol.*, **49**, 553–559.
58. Brown,T.A., Cecconi,C., Tkachuk,A.N., Bustamante,C. and Clayton,D.A. (2005) Replication of mitochondrial DNA occurs by strand displacement with alternative light-strand origins, not via a strand-coupled mechanism. *Genes Dev.*, **19**, 2466–2476.

59. Hamon,L., Pastre,D., Dupaigne,P., Le Breton,C., Le Cam,E. and Pietrement,O. (2007) High-resolution AFM imaging of single-stranded DNA-binding (SSB) protein–DNA complexes. *Nucleic Acids Res.*, **35**, e58.
60. Yang,Y., Sass,L.E., Du,C., Hsieh,P. and Erie,D.A. (2005) Determination of protein-DNA binding constants and specificities from statistical analyses of single molecules: MutS-DNA interactions. *Nucleic Acids Res.*, **33**, 4322–4334.
61. Verhoeven,E.E., Wyman,C., Moolenaar,G.F., Hoeijmakers,J.H. and Goosen,N. (2001) Architecture of nucleotide excision repair complexes: DNA is wrapped by UvrB before and after damage recognition. *EMBO J.*, **20**, 601–611.
62. Hansma,H.G., Revenko,I., Kim,K. and Laney,D.E. (1996) Atomic force microscopy of long and short double-stranded, single-stranded and triple-stranded nucleic acids. *Nucleic Acids Res.*, **24**, 713–720.
63. Luger,K., Mader,A.W., Richmond,R.K., Sargent,D.F. and Richmond,T.J. (1997) Crystal structure of the nucleosome core particle at 2.8 A resolution. *Nature*, **389**, 251–260.
64. Luger,K., Dechassa,M.L. and Tremethick,D.J. (2012) New insights into nucleosome and chromatin structure: an ordered state or a disordered affair? *Nat. Rev. Mol. Cell Biol.*, **13**, 436–447.
65. Raghunathan,S., Kozlov,A.G., Lohman,T.M. and Waksman,G. (2000) Structure of the DNA binding domain of E. coli SSB bound to ssDNA. *Nat. Struct. Biol.*, **7**, 648–652.
66. Lohman,T.M. and Ferrari,M.E. (1994) Escherichia coli single-stranded DNA-binding protein: multiple DNA-binding modes and cooperativities. *Annu. Rev. Biochem.*, **63**, 527–570.
67. Hoke,G.D., Pavco,P.A., Ledwith,B.J. and Van Tuyle,G.C. (1990) Structural and functional studies of the rat mitochondrial single strand DNA binding protein P16. *Arch. Biochem. Biophys.*, **282**, 116–124.
68. Bujalowski,W., Overman,L.B. and Lohman,T.M. (1988) Binding mode transitions of Escherichia coli single strand binding protein-single-stranded DNA complexes. Cation, anion, pH, and binding density effects. *J. Biol. Chem.*, **263**, 4629–4640.
69. Shereda,R.D., Kozlov,A.G., Lohman,T.M., Cox,M.M. and Keck,J.L. (2008) SSB as an organizer/mobilizer of genome maintenance complexes. *Crit. Rev. Biochem. Mol. Biol.*, **43**, 289–318.
70. Roy,R., Kozlov,A.G., Lohman,T.M. and Ha,T. (2009) SSB protein diffusion on single-stranded DNA stimulates RecA filament formation. *Nature*, **461**, 1092–1097.
71. Lohman,T.M. and Bujalowski,W. (1988) Negative cooperativity within individual tetramers of Escherichia coli single strand binding protein is responsible for the transition between the (SSB)35 and (SSB)56 DNA binding modes. *Biochemistry*, **27**, 2260–2265.
72. Roy,R., Kozlov,A.G., Lohman,T.M. and Ha,T. (2007) Dynamic structural rearrangements between DNA binding modes of E. coli SSB protein. *J. Mol. Biol.*, **369**, 1244–1257.
73. Kozlov,A.G., Weiland,E., Mittal,A., Waldman,V., Antony,E., Fazio,N., Pappu,R.V. and Lohman,T.M. (2015) Intrinsically disordered C-terminal tails of E. coli single-stranded DNA binding protein regulate cooperative binding to single-stranded DNA. *J. Mol. Biol.*, **427**, 763–774.
74. Webster,G., Genschel,J., Curth,U., Urbanke,C., Kang,C. and Hilgenfeld,R. (1997) A common core for binding single-stranded DNA: structural comparison of the single-stranded DNA-binding proteins (SSB) from E. coli and human mitochondria. *FEBS Lett.*, **411**, 313–316.
75. Savvides,S.N., Raghunathan,S., Futterer,K., Kozlov,A.G., Lohman,T.M. and Waksman,G. (2004) The C-terminal domain of full-length E. coli SSB is disordered even when bound to DNA. *Protein Sci.*, **13**, 1942–1947.
76. Kozlov,A.G., Cox,M.M. and Lohman,T.M. (2010) Regulation of single-stranded DNA binding by the C termini of Escherichia coli single-stranded DNA-binding (SSB) protein. *J. Biol. Chem.*, **285**, 17246–17252.
77. Morin,J.A., Cerron,F., Jarillo,J., Beltran-Heredia,E., Ciesielski,G.L., Arias-Gonzalez,J.R., Kaguni,L.S., Cao,F.J. and Ibarra,B. (2017) DNA synthesis determines the binding mode of the human mitochondrial single-stranded DNA-binding protein. *Nucleic Acids Res.*, **45**, 7237–7248.
78. Wilson,R.J., Denny,P.W., Preiser,P.R., Rangachari,K., Roberts,K., Roy,A., Whyte,A., Strath,M., Moore,D.J., Moore,P.W. *et al.* (1996) Complete gene map of the plastid-like DNA of the malaria parasite Plasmodium falciparum. *J. Mol. Biol.*, **261**, 155–172.
79. Prusty,D., Dar,A., Priya,R., Sharma,A., Dana,S., Choudhury,N.R., Rao,N.S. and Dhar,S.K. (2010) Single-stranded DNA binding protein from human malarial parasite Plasmodium falciparum is encoded in the nucleus and targeted to the apicoplast. *Nucleic Acids Res.*, **38**, 7037–7053.
80. Antony,E., Weiland,E.A., Korolev,S. and Lohman,T.M. (2012) Plasmodium falciparum SSB tetramer wraps single-stranded DNA with similar topology but opposite polarity to E. coli SSB. *J. Mol. Biol.*, **420**, 269–283.
81. Antony,E., Kozlov,A.G., Nguyen,B. and Lohman,T.M. (2012) Plasmodium falciparum SSB tetramer binds single-stranded DNA only in a fully wrapped mode. *J. Mol. Biol.*, **420**, 284–295.
82. Miralles Fuste,J., Shi,Y., Wanrooij,S., Zhu,X., Jemt,E., Persson,O., Sabouri,N., Gustafsson,C.M. and Falkenberg,M. (2014) In vivo occupancy of mitochondrial single-stranded DNA binding protein supports the strand displacement mode of DNA replication. *PLos Genet.*, **10**, e1004832.
83. Bogenhagen,D.F. and Clayton,D.A. (2003) The mitochondrial DNA replication bubble has not burst. *Trends Biochem. Sci.*, **28**, 357–360.
84. Takamatsu,C., Umeda,S., Ohsato,T., Ohno,T., Abe,Y., Fukuoh,A., Shinagawa,H., Hamasaki,N. and Kang,D. (2002) Regulation of mitochondrial D-loops by transcription factor A and single-stranded DNA-binding protein. *EMBO Rep.*, **3**, 451–456.
85. Chou,Q. (1992) Minimizing deletion mutagenesis artifact during Taq DNA polymerase PCR by E. coli SSB. *Nucleic Acids Res.*, **20**, 4371.
86. Corral-Debrinski,M., Horton,T., Lott,M.T., Shoffner,J.M., Beal,M.F. and Wallace,D.C. (1992) Mitochondrial DNA deletions in human brain: regional variability and increase with advanced age. *Nat. Genet.*, **2**, 324–329.
87. Zeviani,M., Moraes,C.T., DiMauro,S., Nakase,H., Bonilla,E., Schon,E.A. and Rowland,L.P. (1988) Deletions of mitochondrial DNA in Kearns-Sayre syndrome. *Neurology*, **38**, 1339–1346.
88. Krishnan,K.J., Reeve,A.K., Samuels,D.C., Chinnery,P.F., Blackwood,J.K., Taylor,R.W., Wanrooij,S., Spelbrink,J.N., Lightowlers,R.N. and Turnbull,D.M. (2008) What causes mitochondrial DNA deletions in human cells? *Nat. Genet.*, **40**, 275–279.